Neutrophil conversion from a chronic to tumor-killing phenotype underpins effective microbial therapy

Authors:

Andrew O. Yam[1,2,3], Jacqueline Bailey[1], Francis Lin[1], Arnolda Jakovija[1,2], Scott E. Youlten[3], Claudio Counoupas[4], Matthias Gunzer[5], Tobias Bald[6], Trent M. Woodruff[7], James A. Triccas[4], Leonard D. Goldstein[3], David Gallego-Ortega[3,8], Shane T. Grey[1,2], and Tatyana Chtanova[1,9*]

Affiliations:

[1]Immunity Theme, Garvan Institute of Medical Research, Sydney, NSW 2010, Australia

[2]St Vincent's Clinical School, Faculty of Medicine, University of New South Wales Sydney, NSW 2052, Australia

[3]Kinghorn Centre for Clinical Genomics, Garvan Institute of Medical Research, Sydney, NSW, Australia

[4]Discipline of Infectious Diseases and Immunology, School of Medical Sciences, Faculty of Medicine and Health, University of Sydney, Camperdown, NSW 2006, Australia

[5]Institute for Experimental Immunology and Imaging, University Hospital, University Duisburg-Essen, 45147, Essen, Germany

[6]Institute of Experimental Oncology University Hospital Bonn Venusberg-Campus 1, 53127 Bonn, Germany

[7]School of Biomedical Sciences, The University of Queensland, Research Road, St Lucia, Brisbane, Queensland 4072, Australia

[8]School of Biomedical Engineering, Faculty of Engineering and Information Technology, University of Technology Sydney, Ultimo NSW 2007. Australia

[9]School of Biotechnology and Biomolecular Sciences, Faculty of Science, University of New South Wales Sydney, NSW 2052, Australia

The authors declare no potential conflicts of interest.

*Correspondence: Tatyana Chtanova, School of Biotechnology and Biomolecular Sciences, Faculty of Science, University of New South Wales Sydney, NSW 2052, Australia

Email: t.chtanova@unsw.edu.au

ABSTRACT

The inflammatory microenvironment of solid tumors creates a pro-tumorigenic milieu that resembles chronic inflammation akin to a subverted wound healing response. Here we investigated the effect of converting the tumor microenvironment from a chronically inflamed state to one of acute microbial inflammation by injecting microbial bioparticles directly into tumors. This led to rapid and dramatic changes in the tumor immune composition, the most striking of which was a substantial increase in the presence of activated neutrophils. With the aid of *in situ* photoconversion and intravital microscopy, we found that tumor neutrophils transiently switched from sessile producers of vascular endothelial growth factor to highly motile neutrophils that clustered to make neutrophil-rich domains in the tumor. These neutrophil clusters remodeled tumor tissue and repressed tumor growth, demonstrating that one of the major effector mechanisms of microbial therapy is the conversion of tumor neutrophils from a wound healing to an acutely activated cytotoxic phenotype. Single cell analysis of transcription in microbially stimulated neutrophils showed a profound shift in gene expression towards heightened activation and anti-microbial effector function. Microbially activated neutrophils also upregulated chemokines known to regulate neutrophil and T cell recruitment. Microbial therapy also boosted CD8 T cell function and the therapeutic benefit of checkpoint inhibitor therapy in both primary and recurrent tumor models. These data highlight a rationale for broader deployment of microbial therapy in the treatment of solid cancers.

INTRODUCTION

Most solid tumors generate a sub-acute inflammatory response that favors a pro-tumorigenic milieu and recruits leukocytes that contribute to angiogenesis, tumor growth and suppression of anti-tumor immunity (1). In contrast, as was first observed by William B. Coley in the 1890s, certain microbial preparations can shift the balance in the tumor microenvironment (TME) towards an acute inflammatory response that can inhibit cancer growth (2). Indeed, bladder cancer micrometastases have been successfully eradicated by treatment with *Mycobacterium bovis* Bacillus Calmette Guerin (BCG) (3). Yet why some cancers are sensitive to acute inflammation despite being promoted by chronic inflammation is not understood (4), but the answer to this question may hold clues to how successfully deploy inflammation in cancer therapy.

Several microbial and toll-like receptor (TLR) adjuvants are currently in clinical trials for various solid cancers (5). However, so far, their success in the clinic as cancer monotherapies has been limited, suggesting that a better understanding of microbe-triggered acute inflammation in cancer is required to enable broader application of microbial adjuvants as cancer therapy. To date, most of the investigations of microbial therapy have been focused on the changes in antigen presentation capacity of dendritic cells (DCs) and macrophage activation (5). Yet there are many immune cell types known to respond to microbial stimulation. The role of neutrophils in mediating the anti-cancer effect of microbial therapies has not been explored in detail despite several studies demonstrating neutrophil recruitment in response to BCG (3,6).

Neutrophils are an essential first line of immune response to microbes but are also a common component of the TME of solid cancers (7), where they can support cancer development and are associated with a poor prognosis (8). Neutrophils can promote tumor growth by stimulating tumor angiogenesis (8,9) and by producing molecules that suppress anti-tumor immune responses (10-12). Tumor-infiltrating neutrophils can aid metastasis (13-15) and impair the effectiveness of anti-tumor immune therapies by establishing a pro-tumor immunosuppressive microenvironment (16-19).

Neutrophils can also have potent anti-tumor functions including direct cytotoxicity against tumor cells and attenuation of metastasis (20-22). Increased neutrophil infiltration in a model of colon adenocarcinoma had potent anti-tumor effects mediated in part through cross-talk with CD8 T cells (23)(24). The opposing roles for neutrophils in cancer led to the development of the N1/N2 paradigm, where N1 neutrophils have anti-tumor properties, whereas N2 neutrophils are tumor promoting. Notably, pro-tumor N2 neutrophils can be converted into N1 anti-tumor effectors by modulating the TME (25), though the mechanisms that govern the switch between N1 anti-tumor and N2 pro-tumor neutrophils are poorly understood. The ability of neutrophils to take on pro- or anti-tumor function highlight that these cells rely on external cues in the TME to determine their activation and phenotypic

state. How anti-tumor neutrophils interact with tumor cells and how their anti-tumor functions can be maintained are all unknown but could reveal how to manipulate them to achieve an anticancer benefit.

Here, we show that a key consequence of switching the type of inflammation within tumors from chronic to acute using microbial bioparticles, is the conversion of neutrophils from a wound healing to a tumor-killing phenotype. Microbe activated (MA) neutrophils demonstrated a unique tumor-toxic capacity and provided a strong anti-cancer effect. Single cell analysis of gene expression in MA neutrophils showed that they induced a distinctive gene expression program associated with bacterial activation, effector function and migration. They also regulated tumor immunity by producing chemokines that recruit neutrophils as well as T cells into tumors. Concordantly, we observed enhanced CD8 T cell immunity, protection upon tumor rechallenge and increased checkpoint inhibitor efficacy. Our findings identify neutrophil-mediated anti-tumor mechanisms associated with a switch from chronic to acute inflammation in the TME and highlight neutrophil-based approaches to successfully target inflammation in cancer therapy.

RESULTS

Switching the TME from chronic to acute inflammation reshapes the immune landscape

We first investigated how converting the TME from chronic to acute anti-microbial inflammation would alter the tumor immune landscape. To track immune cell function *in vivo* we established Lewis Lung Carcinoma (LLC) tumors in the ear pinnae of C57Bl/6 mice. This model, which we developed for an earlier study (26), allows *in vivo* analysis of tumor immune infiltrates by *in situ* photoconversion and intravital microscopy without inflammation-inducing surgical procedures.

Analysis of unmanipulated tumors 10-14 days after inoculation shows an evident leukocyte infiltration (**Fig. 1A, Supplementary Fig. 1A, B**). Injection of *Staphylococcus aureus* (*S. aureus*) bioparticles directly into tumors led to a striking increase in the immune cell infiltration (**Fig. 1A and Supplementary Fig. 1A, B)**. We observed increased recruitment of monocytes and DCs, but the proportions of migratory DCs, cDC1 and cDC2 subsets (**Supplementary Figs. 2, 3A-D**) remained unchanged after treatment. The number of macrophages (**Supplementary Fig. 3A**) and the proportions of F4/80+ and MHC class II^{high} subsets were also unaltered (**Supplementary Figs. 3E, F**).

Among lymphocytes, the number of B cells was unchanged, while the number of $CD3^+$ T cells increased in treated tumors (**Supplementary Fig. 3G, H**). This increase was due to an increase in $CD4^-CD8^-$ rather than conventional $CD8^+$ or $CD4^+$ T cells (**Supplementary Fig. 3I**). Unlike CD4-CD8- T cells in autoimmune conditions (27), only a very small proportion of tumor CD4-CD8- T cells were B220+ and this proportion did not change following microbial treatment (**Supplementary Fig. 3J)**.

The biggest change in tumor infiltrating immune subsets after microbial treatment was the 28-fold increase in neutrophils (identified as $Ly6G^+CD11b^+$ cells) in treated tumors (**Fig. 1B, Supplementary Figs. 1C, 3K**). Neutrophils comprised ~20-40% of all immune cells in the untreated tumors but made up more than 85% of the tumor immune infiltrate following microbial treatment (**Fig. 1C**). Although neutrophil marker Ly6G can, in some settings, be expressed on eosinophils (28) and eosinophil blood counts in patients have been linked to disease recurrence during BCG treatment (29), we did not observe significant changes in eosinophil number in tumors or peripheral blood of mice treated with microbial bioparticles (**Supplementary Figs. 3L, M**). Furthermore, only a small subset of Ly6G+CD11b+ cells in tumors co-expressed the eosinophil markers SiglecF and F4/80 following microbial stimulation (**Supplementary Fig. 3N**). These results demonstrate that microbial bioparticle treatment dramatically re-shapes the tumor immune landscape promoting recruitment of immune cells, and especially neutrophils, into tumors.

Microbial therapy leads to a switch in neutrophil phenotype and function

To investigate how the change in the TME alters neutrophil state, we examined the phenotype of tumor neutrophils. We found similar levels of Gr-1 (Ly6G/Ly6C, a marker of G-MDSC cells) on total Ly6G+ and intermediate cells in control and *S. aureus*-treated tumors (**Supplementary Fig. 3O**). Furthermore, neutrophil maturity (assessed by the expression of Ly6G and CXCR4 (30)) was similar in tumors prior to injection of microbial therapy, at 8 hours (when many infiltrating neutrophils have recently entered the tumor) and 24 hours after *S. aureus* treatment (**Supplementary Fig. 3P**). The majority of tumor neutrophils across all conditions had a mature ($Ly6G^{high}CXCR4^{lo}$) phenotype with only a small number of neutrophils of intermediate maturity.

Next, we assessed the expression of CD11b, CD62L and CXCR2, which are regulated upon neutrophil activation (31-33). Consistent with the neutrophil phenotype in response to a bacterial stimulus (34), microbial treatment led to an increase in the activation marker CD11b and concomitant downregulation of CD62L and CXCR2 (**Fig. 1 D-F**).

When we examined neutrophil function following microbial treatment, neutrophils were the main immune subset to phagocytose microbial particles (assessed by uptake of labeled *S. aureus* bioparticles, **Fig. 1G**). Neutrophils in unmanipulated tumors expressed higher levels of vascular endothelial growth factor (VEGF), which is involved in angiogenesis and wound healing and is considered a pro-tumor molecule due to its ability to promote tumor growth and metastasis (9) (**Fig. 1H**). While MMP9 and MPO (**Fig. 1 I, J**) were not significantly altered following treatment, we observed an increase in the levels of inducible nitric oxide synthase (iNOS) (**Fig. 1K**), an anti-microbial agent produced in response to phagocytosis that can also stimulate apoptosis and kill nearby cells by releasing reactive oxygen species (ROS) (21,35). These data show that microbial treatment polarizes the phenotype of tumor neutrophils to one characteristic of an anti-microbial response.

Microbial bioparticle treatment alters intratumoral neutrophil dynamics

Next, we leveraged intravital two-photon microscopy to visualize neutrophil dynamics within intact tumors established in neutrophil-specific reporter ($BigRed/Catchup^{IVM\text{-}red}$) mice where tdTomato fluorescent protein is expressed in $Ly6G^{+}$ neutrophils (36). Prior to treatment, neutrophils which were scattered throughout the tumor mass (**Fig. 2A**), displayed limited motility (median average speed 0.04 μm/second) and displacement (median displacement 3 μm) (**Figs. 2B,C, Supplementary Video 1**), unlike neutrophils responding to acute microbial inflammation which migrate rapidly to coalesce in dynamic swarms (37). However, neutrophil dynamics and distribution rapidly changed following microbial treatment. As early as 4 hours after treatment, we detected large clusters of neutrophils throughout the tumor mass (**Fig. 2A**) and a 2.5-fold increase in neutrophil speed and a 4-fold increase in displacement (**Figs. 2B, C, Supplementary Video 1)**.

When we adoptively transferred fluorescently labelled bone marrow cells into tumor bearing mice, we observed recruitment of labeled neutrophils into tumors and this recruitment substantially increased after microbial injection (**Supplementary Fig. 4A**), indicating that circulating neutrophils exported from the bone marrow are recruited into tumors. We confirmed that the time spent in the TME was not driving the change in neutrophil motility by showing that neutrophils adoptively transferred at two different times had similar motility in unmanipulated tumors (**Supplementary Fig. 4B**). This indicates that the changes in neutrophil motility are driven by the microbial stimulus.

The increase in neutrophil motility was transient and by 24 hours after microbial treatment neutrophil speed started to decline. Detailed analysis of neutrophil dynamics 24 hours post treatment revealed two distinct modes of behavior, where a proportion of neutrophils remained motile, while most neutrophils formed large stable clusters of low motility (**Fig. 2A**, **Supplementary Video 1**). Our results show that neutrophil dynamics in the chronically inflamed TME are profoundly different to those in acute inflammation – MA neutrophils displayed increased motility and formed large clusters within the tumor mass indicating a change in how neutrophils interact with tumor cells.

MA neutrophils remodel tumor matrix

To test whether MA neutrophils carry out tumor remodeling *in vivo* similarly to tissue remodeling mediated by neutrophil swarms in response to infectious and sterile inflammation (37,38), we set up a model to investigate neutrophil interactions with tumor cells in intact LLC-eGFP tumors established in the ear pinnae of neutrophil reporter mice. Within 24 hours following microbial bioparticle treatment, large neutrophil clusters could be observed within the tumor mass (**Fig. 3A**). Notably, these clusters corresponded to areas cleared of tumor cells and collagen indicating that MA neutrophils in treated tumors remodel tumors.

Next, we applied intravital imaging to examine the interactions between neutrophils and GFP-tagged tumor cells in real time. In contrast to elongated intact LLC cells in unmanipulated tumors, we observed an increase in rounded tumor cells and tumor cell debris in areas of neutrophil infiltration in microbe-treated tumors, (**Fig. 3B, Supplementary Video 2**). Quantitation of eGFP signal showed loss of LLC tumor cells in treated tumors (**Fig. 3B)**. We tested whether microbial stimulation enhances neutrophil capacity to kill tumor cells by incubating LLC cells with purified neutrophils and *S. aureus* bioparticles or unstimulated neutrophils *in vitro* and found that that LLC cells incubated with microbe-activated neutrophils for 24 hours showed significantly more cell death (**Fig. 3C)**.

When we visualized neutrophil-tumor cell interactions over time, we observed that neutrophils engaged in multiple interactions with tumor cells (**Fig. 3D, Supplementary Video 3**). We found that neutrophil motility was significantly lower in areas of tumor remodeling where a large number of rounded tumor cells was observed (**Fig. 3E)**. Our analysis revealed tumor cells within neutrophil

clusters undergoing blebbing, a characteristic feature of cell death (**Fig. 3F**, **Supplementary Video 4)**. We used labeling with SYTOX to confirm tumor cell death within neutrophil clusters (**Fig. 3G)**. Taken together our results indicate that MA neutrophils remodel tumor matrix and may contribute to tumor cell death.

NETs are induced in response to microbial therapy

Neutrophil Extracellular Traps (NETs) are one of the mechanisms of neutrophil pathogen defense but have also been observed in sterile inflammation (31). In cancer, NETs play a role in tumor metastasis and tissue remodeling (39). We stained tumor sections for citrullinated histone H3 and neutrophil elastase to detect NETs and observed a significant increase in both markers within tumors after microbial treatment (**Supplementary Fig. 5A)**. To test whether inhibiting NETosis in the TME would affect neutrophil recruitment and function in response to *S. aureus*, we administered GSK484, a potent and reversible inhibitor of Protein Arginine Deiminase 4, which inhibits the formation of NETs in both mouse and human neutrophils (40). Our analysis showed that GSK484 administration did not alter neutrophil recruitment to tumors in response to *S. aureus*, nor their functions including iNOS, MMP9 and MPO **(Supplementary Figs. 5B-D)**. Finally, we employed two-photon microscopy (as in **Fig. 3A, B**) to assess the extent of tissue remodeling and loss of GFP cells when *S. aureus* was co-administered with GSK484. We found no significant changes in tumor remodeling after NETosis was inhibited in microbe-treated tumors (**Supplementary Fig. 5F)**, indicating that factors other than NETosis contribute to neutrophil tumor remodeling in response to microbial therapy.

Microbe- and tumor-derived signals shape neutrophil phenotype and turnover

Our data suggest that microbial bioparticle treatment converts neutrophils into anti-tumor effectors. To investigate whether the stimulatory effect of microbial bioparticles persists over a prolonged period or is suppressed by the TME, we examined neutrophil number and activation over time. Following rapid recruitment in response to microbial treatment, intratumoral neutrophil number remained stable over the course of 72 hours (**Fig. 4A**). In contrast, neutrophil activation rapidly decreased as evidenced by a decline in the expression of CD11b (**Fig. 4B**), suggesting that repeated stimulation is required to maintain the acutely activated tumoritoxic phenotype.

To examine the changes in neutrophil phenotype when subjected to signals within the TME, we took advantage of a photoconversion-based approach that we have developed to label tumor-infiltrating immune cells (26), and used it to compare the phenotypes of tumor-experienced neutrophils to neutrophils in circulation and neutrophils recently recruited to tumors. Our analysis showed that as neutrophils left circulation and infiltrated tumors, they became activated (as indicated by increased expression of CD11b and downregulation in CD62L and CXCR2, **Fig. 4C-E**). Notably, this

activation was more pronounced in photoconverted tumor-experienced neutrophils compared to non-photoconverted recently recruited neutrophils, indicating that circulating neutrophils undergo progressive activation upon entering tumors.

When we examined the effect of microbial bioparticle treatment on phenotype of recently-recruited and tumor-experienced neutrophils, we found that neutrophil activation was enhanced by *S. aureus* bioparticles (**Fig. 4C-E**). However, tumor-experienced neutrophils appeared less susceptible to stimulation since *S. aureus* treatment did not alter CD11b and CD62L levels on photoconverted neutrophils, suggesting that aged neutrophils lose some of their plasticity and ability to respond to signals in their environment.

We next used the photoconversion system to analyze the expression of chemokine receptor CXCR4, which is associated with neutrophil migration and aging (41,42). As expected, CXCR4 expression was higher in photoconverted neutrophils that are likely to be more aged than non-photoconverted neutrophils that have recently entered the tumor from circulation (**Fig. 4F**). CXCR4 expression was unchanged in neutrophils from microbial particle-treated tumors suggesting that tumor neutrophils rapidly acquire an aging phenotype regardless of microbial signals.

Neutrophils are short-lived cells with a half-life of just several hours in circulation (43). Their lifespan can be extended to several days when neutrophils enter tissues (31), but how long they survive in the TME is not yet known. To address this knowledge gap, we used photoconversion to label neutrophils in tumors and analyze the number of photoconverted neutrophils remaining in tumors at various timepoints. We observed a sharp decline in the number of photoconverted neutrophils in tumors over time – neutrophil number decreased by 63% between 24 and 48 hours and by 92% between 48 and 72 hours (**Fig. 4G**), indicating that most tumor-infiltrating neutrophils do not survive for extended periods of time. However, the decline in photoconverted neutrophils was less rapid following *S. aureus* injection with neutrophil number decreasing by 37% between 24 and 48 hours and by 74% between 48 and 72 hours (**Fig. 4G**), suggesting that microbial activation prolongs tumor neutrophil survival.

Neutrophil turnover in tumors is contributed to by the influx of neutrophils into tumors and death *in situ*. Whether neutrophils can also emigrate from tumors has not been examined. We applied photoconversion as previously (26) to assess neutrophil egress from tumors to draining lymph nodes. By photoconverting tumor-infiltrating cells prior to microbial bioparticle treatment and then analyzing draining lymph nodes for the presence of photoconverted tumor-egressing neutrophils, we found that neutrophils emigrated poorly from unmanipulated tumors (**Fig. 4H**). However, microbial bioparticle treatment substantially increased egress of photoconverted neutrophils to draining lymph nodes (**Fig. 4H**). Taken together our data indicate that microbial treatment modulates neutrophil

turnover within the TME and trafficking from tumors. These results also highlight that the stimulatory effect of microbial therapy on neutrophil activation is transient and that neutrophil phenotype quickly evolves in response to the TME.

Microbial treatment inhibits tumor growth

Microbial treatment with killed *S. aureus* bioparticles led to substantial neutrophil influx into tumors and a switch in neutrophil function (**Fig. 1**). Coupled with our intravital imaging results showing that MA neutrophils remodeled large areas within tumors and destroyed tumor cells (**Fig. 3**), this suggested that these neutrophils may have a potent anti-tumor effect. However, analysis of neutrophil activation over time showed a rapid peak and loss of activation (**Fig. 4**), indicating that repeated stimulation is required to maintain the acute phenotype and neutrophil anti-tumor function. Consistent with this, we observed that a single injection of microbial bioparticles was not sufficient to repress tumor growth (6 out 7 mice treated once reached ethical endpoints for tumor size within 3 weeks). Therefore, we assessed whether repeated microbial treatment could repress tumor growth by comparing the volume of LLC tumors that were treated with microbial bioparticles on alternate days or vehicle control or untreated tumors. In the unmanipulated (or vehicle treated) state LLC tumors show an exponential growth pattern up to 2-3 weeks post-inoculation at which point animals reach ethical endpoints and are euthanized (**Fig. 5A**). However, we observed a striking suppression of tumor growth after treatment with *S. aureus* microbial bioparticles (**Fig. 5A**). This shows that treatment with microbial bioparticles could override the normally pro-tumorigenic TME to promote a potent anti-tumor response.

To demonstrate that this is a broad phenomenon not restricted to a specific cancer model, we tested our microbial treatment in the B16F10 melanoma model but also in the AT-3 model of triple negative breast cancer and KPC model of pancreatic ductal adenocarcinoma since these cancers are considered to be 'cold' cancers refractory to immune attack and resistant to checkpoint immunotherapy (44,45). Remarkably, in these models, microbial particle treatment again substantially inhibited tumor growth (**Supplementary Figs. 6A-C**), indicating that our microbial bioparticle treatment approach is effective in a range of solid tumors and has potential utility for cold cancers like pancreatic cancer for which few effective therapies exist (46).

Tumor growth inhibition achieved by treatment with *S. aureus* bioparticles suggested that microbial activation may represent a common mechanism by which anti-tumor neutrophils can be recruited. Administration of BCG is in clinical practice to eradicate micrometastases in bladder cancer, although its mechanism of action is unclear (3). We investigated whether administration of BCG can modulate tumor growth in C57Bl/6 mice. As was observed with *S. aureus* bioparticles, intratumoral treatment with BCG led to both a rapid influx of neutrophils (**Supplementary Fig. 7**) and substantial

suppression of tumor growth (**Fig. 5B**). These data demonstrate that the effect of microbial treatment on tumor growth is not restricted to particular microorganisms like *S. aureus,* but represents a general principle of microbe-mediated tumor growth control.

Neutrophils are required for tumor growth inhibition

To determine whether MA neutrophils provide a causal contribution to the control of tumor growth in response to microbial treatment, we treated LLC-bearing mice with *S. aureus* bioparticles to suppress tumor growth but also depleted tumor-infiltrating neutrophils using neutrophil-specific anti-Ly6G antibody (**Supplementary Fig. 8**). Although neutrophils are hard to deplete long-term due to their rapid replenishment by the bone marrow (47), short-term neutrophil depletion reversed the tumor suppression effect of *S. aureus* (**Fig. 5C**). These data demonstrate that MA neutrophils are essential for microbe-mediated inhibition of tumor growth.

Neutrophil anti-tumor capability is determined by their kinetics in tumors

Our analysis of neutrophil recruitment kinetics showed that neutrophil numbers are maintained for at least 3 days following microbe inoculation while neutrophil activation declines over the same period (**Fig. 4A**, **B**). This suggests that restimulation of intratumoral neutrophils during their peak recruitment period to boost their anti-tumor function and maintain the acute phenotype, as well as recruitment of non-conditioned neutrophils from circulation, would be beneficial. Consistent with this hypothesis, analysis of tumor growth over time showed that extending treatment of tumors to every 4 days could inhibit tumor growth (**Supplementary Fig. 6D**). This suggests that an effective microbial treatment regime could be developed based on the kinetics of neutrophil phenotype switching.

CD8 T cells are co-effectors of microbial therapy

To test whether adaptive immunity, specifically CD8 T cells, also contribute to the anti-tumor effect of microbial therapy, we administered *S. aureus* bioparticles as previously but also depleted CD8 T cells. Analysis of tumor growth over time showed that the tumor growth inhibitory effect of microbial therapy was lost in the absence of CD8 T cells (**Fig. 5D**), indicating that CD8 T cells are important mediators of the anti-tumor effects of microbial therapy.

Mechanisms of microbe-mediated tumor growth inhibition

The increase in cytotoxicity coupled with iNOS upregulation suggests that the release of ROS following microbial activation is a potential mechanism for tumor cell killing by microbially activated neutrophils. We used N-*acetylcysteine* (*NAC*) to inhibit ROS *in vivo* and observed that administration of NAC on its own significantly increased the rate of tumor growth (**Fig. 5E**). Notably, while anti-cancer potential of antioxidants has been recognized for some time, several recent studies have shown

that blocking ROS and specifically, administering NAC in vivo can also have pro-tumor effects (48-50). This effect of NAC on tumors makes it hard to interpret the effect of co-administration of microbial therapy and NAC. However, our results show that suppressing ROS using NAC is insufficient on its own to inhibit the anti-tumor effect on microbial therapy.

Previous studies reported that neutrophils can kill antibody-coated tumor cells via tropotosis (51). We did not observe transfer of cancer cell plasma membrane to neutrophils, indicating that unlike ADCC-mediated cancer cell death, tumor cell death did not occur by neutrophil trogocytosis. We wanted to test whether complement is involved in mediating the anti-tumor effects of microbial therapy. Analysis of tumor sections following microbial treatment detected a significant increase in complement C1q expression (**Supplementary Fig. 9**). This suggests that complement activation and tumor cell opsonization may contribute to tumor cell removal following microbial therapy. As complement activation generates the potent neutrophil mobilizer and chemotaxin, C5a (52), we tested the role of this complement factor in tumor growth control in response to microbial treatment, using the C5a receptor (C5aR1) antagonist PMX205 (52) (**Fig. 5F**). We found that daily intraperitoneal administration of the inhibitor did not significantly alter tumor growth in vivo and when administered in combination with microbial therapy did not affect tumor growth suppression effect of microbial therapy, suggesting that blocking the complement C5a pathway is insufficient on its own to inhibit neutrophil anti-tumor functions.

Microbial therapy redirects tumor neutrophil transcriptional program

To investigate how neutrophils in the TME respond to microbial stimulation at the level of transcription, we conducted single cell gene expression analysis of tumor infiltrating $Ly6G^{+}CD11b^{+}$ neutrophils isolated from unmanipulated tumors or tumors treated with a vehicle control (control) or *S. aureus* bioparticles (stimulated) for 24 hours (**Supplementary Figs. 10A, B**). To survey the whole spectrum of the TME we also isolated and sequenced non-neutrophil leukocytes in each sample. After quality control we obtained 7729 (stimulated), 5226 (control), and 3895 (unmanipulated) high-quality cells with an average of 2042 genes per cell and a total of 20950 genes detected across all conditions. Each condition contained a prominent population of neutrophils among other leukocyte populations, including basophils and eosinophils, macrophages, DCs, B, T and NK cells within our samples (**Fig. 6A)**. Consistent with previous reports of lower RNA content and transcriptional activity in neutrophils compared to other immune subsets (53,54), we observed lower transcript counts and fewer genes detected per cell but a higher percent of counts in the top 50 most highly expressed genes in neutrophils when compared to other tumor immune subsets (**Supplementary Fig. 10C)**.

We identified five distinct transcriptional states in the TME neutrophils, Neu1-Neu5 (**Fig. 6B)**. These states segregated closely with treatment condition and were robust to *in silico* batch correction (**Fig.**

6C, Supplementary Fig. 10E). Neutrophils from tumors stimulated with *S. aureus* bioparticles almost exclusively form two distinct states, Neu1 and Neu2 (respectively 99.5% and 97.5% of cells) **(Fig. 6D)**. In contrast, neutrophils from unmanipulated tumors (96%) were mostly contained within the Neu5 cell cluster. The majority of neutrophils in Neu4 were from vehicle control tumors (91%), while Neu3 was a mix of neutrophils from vehicle and unmanipulated tumors (24% and 71% respectively). This indicates that neutrophils in the TME undergo a profound change in their transcriptional state in response to microbial stimulation.

Transcriptome diversity differed between neutrophil expression states. While total transcript counts were comparable between Neu1-Neu5, fewer genes were detected in Neu1 and Neu2 compared to Neu5 (**Supplementary Fig. 10D)**. Also, compared to Neu5, Neu1-Neu2 had a higher percent of transcripts in the top 50 most highly expressed genes suggesting that *S. aureus* activated neutrophils strongly upregulate a specific subset of highly expressed genes. We hypothesized that the greater transcriptome diversity in the unstimulated Neu5 neutrophils may reflect a less mature phenotype, yet to specialize towards an effector state. Consistent with this, Neu5 had the lowest maturation score (55) compared to all other clusters (**Supplementary Fig. 10F)**. Conversely, the neutrophils responding to *S. aureus* in Neu1/Neu2 had a transcriptional profile consistent with mature neutrophils.

To further characterize the function of neutrophil states, we identified marker genes for Neu1-Neu5 and determined biological processes enriched among them (**Fig. 6E, F, Supplementary Table 1**). Neu1 and Neu2, consisting of *S. aureus*-stimulated neutrophils, upregulated genes associated with an acute response to bacterial infection (**Fig. 6F**). Among the top markers for Neu1 were mediators of neutrophil effector function such as the inducible nitric oxide synthase gene *Nos2* involved in cell killing by ROS generation, as well as antimicrobial granule proteins Lipocalin 2 (*Lcn2*) and Chitinase-like 1 (*Chil1*) (**Fig. 6E**). Neu2 was enriched for genes involved in cytokine-mediated signaling, and top markers included several members of the CXC chemokine family (*Cxcl2*, *Cxcl3*, *Cxcl10*). Neu4, consisting mostly of neutrophils after treatment with vehicle control, was enriched for genes associated with leukocyte adhesion to vascular endothelium, with intercellular adhesion molecule 1 (*Icam1*) among top markers. Neu3, enriched for neutrophils from unmanipulated and control conditions, expressed genes associated with cell migration including Resistin-like gamma precursor (*Retnlg*) and Ccl6. Notably, Neu5 was enriched for genes associated with eicosanoid biosynthesis (prostaglandins and leukotrienes) (**Supplementary Table 1**) including prostaglandin-endoperoxide synthase 1 (*Ptgs1*) as one of the top markers, suggesting that these neutrophils may modulate the chronic inflammatory response in the TME.

Cytokine secretion, chemotaxis and migration were among few processes regulated by most

neutrophil states (**Fig. 6F)**, suggesting that changes in transcription underpin the changes in neutrophil behavior following microbial therapy administration that we observed using intravital microscopy (**Fig. 2)**. Notably, Neu2 and Neu3 most strongly regulated genes associated with migration (**Fig. 6F, G**) but while Neu3 expressed several receptors that mediate neutrophil recruitment (*C5ar2* and *Cxcr2*), Neu2 upregulated a number of chemokines relative to unstimulated neutrophils including *Cxcl2*, *Cxcl3*, *Cxcl10, Ccl3* and *Ccl4* **(Fig. 6H)**. The induction of neutrophil recruiting chemokines *Cxcl2* and *Cxcl3* (56) following *S. aureus* stimulation suggests that one of the mechanisms of maintaining neutrophil numbers in tumors following microbial therapy is via neutrophils themselves. On the other hand, Cxcl10 as well as Ccl3 and Ccl4 have been shown to stimulate NK and CD8 T cell recruitment to tumors (57) suggesting that neutrophil microbial activation in tumors may promote subsequent adaptive immunity. Conversely, *Ccl6*, which binds to CCR1 and is thought to promote tumor metastasis (58), was most highly expressed by Neu3 neutrophils. This indicates that potent immune modulatory cytokines differentiate neutrophil states in tumors and may regulate recruitment of distinct immune subsets. Together, this shows that neutrophils in the TME acquire a mature effector transcriptional state upon *S. aureus* stimulation that may create a distinct tumor immune microenvironment through differential regulation of cytokines.

Activation of adaptive immunity in response to microbial therapy

Single cell gene expression analysis of neutrophils following microbial treatment showed that microbial therapy promoted expression of chemokines involved in T cell recruitment (**Fig. 6G)**. Furthermore, depletion of CD8 T cells demonstrated that these cells are important co-effectors of microbial therapy. Therefore, we assessed T cell recruitment, activation and effector function after two rounds of microbial therapy administered forty-eight hours apart and found increased recruitment of activated T cells in tumors (**Fig. 7A, B**) and draining lymph nodes (**Fig. 7I, J**). Detailed analysis of CD8 T cell function showed augmented numbers of effector CD8 T cells expressing of IFN-γ (**Fig. 7C**), perforin (**Fig. 7D**), granzyme (**Fig. 7E,** trend) and CD107a (**Fig. 7F**) in tumors. Similarly, CD8 effector T cells were increased in draining lymph nodes (**Fig. 7K-M**). The exhaustion markers PD-1 and Tim-3 were increased on tumor infiltrating CD8 T cells ((**Fig. 7G, H**) but not on those in draining lymph nodes (**Fig. 7O and P**). Taken together these indicate that CD8 T cell effector function is enhanced both in tumors and draining lymph nodes in response to microbial therapy.

Microbial treatment synergizes with checkpoint inhibitor therapy

Acquisition of CD8 T cell effector function suggests that microbial therapy may improve the effectiveness of T cell-based immune therapies, such as checkpoint inhibition. To test this, we used the AT-3 tumor model and administered three rounds of *S. aureus* bioparticles intratumorally in combination with checkpoint inhibitors anti-PD1 and anti-CTLA4. Compared to mice that received

checkpoint inhibitor antibodies only, we found that microbial bioparticles significantly enhanced suppression of tumor growth by checkpoint inhibitors (**Fig. 7Q**).

Since tumor recurrence represents a major clinical challenge, we asked whether microbial therapy would improve therapeutic outcomes in a model of tumor recurrence. Mice were inoculated with AT-3 tumor cells and treated with microbial therapy to repress tumor growth, then rested for at least 60 days and subsequently rechallenged with AT-3 tumor cells. We found that in the absence of any additional microbial treatment, mice that were previously treated with microbial therapy successfully suppressed tumor growth compared to naïve mice (**Fig. 7R**). Together these results indicate that microbial therapy can induce an effective CD8 T cell response and enhance the therapeutic impact of checkpoint immunotherapy.

DISCUSSION

The future of cancer immunotherapy depends on understanding the interactions between cancer-associated inflammation and anti-tumor immunity. Here we show that changing the TME from a chronic, aberrant wound healing response to an acute microbe-triggered inflammation induces extensive changes in gene expression, migration and function of tumor neutrophils and ultimately represses tumor growth in a neutrophil-dependent manner.

When neutrophils were first visualized in the context of microbial infection with *Toxoplasma gondii*, they were observed to migrate rapidly between localized foci of inflammation to form dynamic swarms, which remodeled underlying tissue (37,38,59-61). In contrast, tumor neutrophils were either slow moving or sessile but increased their motility following microbial therapy and formed large clusters around tumor cells indicating that microbial signals in the TME induced neutrophils to take on some of the features of the anti-microbial response in tissues. Concomitantly, their function shifted from VEGF production to release of ROS, which is consistent with a transition from wound repair to tumor killing. Neutrophil clusters in treated tumors corresponded to areas cleared of collagen and tumor cells, suggesting that MA neutrophils mediated tumor remodeling by removing tumor cells.

The remarkable tumor growth inhibition achieved by treatment with both *S. aureus* bioparticles and BCG supports a general principle whereby microbial therapy switches neutrophils from a wound healing program to a potent cytotoxic response. Despite its weakened state, live attenuated BCG has the potential to cause disseminated mycobacterium infection in patients (62) so using killed bacterial bioparticles may represent a safer alternative especially for immunocompromised patients. TLR agonists such as TLR3 and TLR9 agonist formulations can stimulate DC maturation and enhance CD8 T cell responses (63) but show only limited clinical efficacy as monotherapies (5). This may reflect the existence of multiple non-redundant pathways that have to be targeted simultaneously to improve clinical efficacy. Further, TLR3 and TLR9 agonists as stand-alone therapies (or as vaccine adjuvants) may be insufficient to overcome immunosuppression mediated by other immune subsets. Microbial therapy successfully inhibited tumor growth in several pre-clinical tumor models, including immunologically cold breast and pancreatic cancers (44,45), indicating that neutrophil plasticity in cancer could be exploited across a range of solid tumors. Our work supports the use of killed microbes as a promising strategy to target multiple TLRs and ensure robust activation of a broad range of immune subsets.

We used photoconversion to dissect neutrophil plasticity in the TME and show that bioparticle-driven switch in neutrophil phenotype was transient and restimulation was required to maintain neutrophils in the anti-tumor state and repress tumor growth. Our data indicate that neutrophils mediate their anti-tumor function by coopting anti-microbial effector mechanisms, such as ROS release, against tumor

cells and link neutrophil tumorotoxic capabilities to the efficacy of bacterial therapy. This suggests pathways for optimizing the effectiveness of microbial therapies by manipulating neutrophil activation to sustain their anti-tumor capabilities and capacity to destroy tumor cells. These have important implications for clinical application of microbial therapy, which could provide benefit as neoadjuvant therapies to shrink solid tumors prior to surgery, as adjuvant therapy to remove residual cancer cells and as a way of reducing inoperable tumors. Although tumor accessibility can limit the scope of intra-tumoral injections, image-guided procedures may provide an opportunity to target less accessible tumors. There are currently several clinical trials utilizing intratumor injections in non-superficial cancers such as pancreatic (source: https://clinicaltrials.gov). Advances in structural chemistry may also permit depot formulations that maintain efficacy with fewer injections with the eventual goal of broadening the use of microbial therapy. Delivery platforms such as the bacterially derived nanocells (64) can be used to deliver microbial therapy to poorly accessible tumors or to tumors that spread to multiple sites where an intravenous delivery system would be advantageous.

Single cell analysis of gene expression showed that the switch in neutrophil functional state induced by microbial therapy was underpinned by a substantial change in their transcription. In response to microbial treatment tumor neutrophils upregulated genes associated with immune activation and microbial defense. Our analysis also revealed that MA neutrophils upregulated expression of chemokines that recruit neutrophils as well as NK and CD8 T cells, suggesting these neutrophils contribute to tumor immunity by shaping the TME to enhance recruitment of anti-tumor lymphocytes, highlighting the importance of understanding neutrophil dynamics as they relate to anti-tumor T cell responses.

Immune suppression mediated by cancer and immune cells is a key obstacle for an effective T cell anti-tumor response. Successive administration of microbial bioparticles led to an increase in effector CD8 T cells in tumors and draining lymph nodes and significantly enhanced the efficacy of checkpoint inhibitor therapy, suggesting that combination strategies targeting both innate and adaptive immunity may synergize to overcome checkpoint blockade resistance and promote tumor killing. Furthermore, microbial treatment of primary tumors conferred protection in a rechallenge model indicating that microbial therapy-mediated tumor repression may establish a protective memory response. Therefore, microbial therapy may provide a pathway to increase adaptive immune responses in poorly infiltrated cancers (e.g., breast or pancreatic cancers), where insufficient immune infiltration and immunosuppression have been major obstacles for checkpoint inhibitor therapy. This substantially expands potential applications of microbial immunotherapy in treatment of solid tumors.

MATERIALS AND METHODS

Mice

All mice used in this study were maintained on C57BL/6 (RRID:MGI:5656552) background and housed in specific pathogen-free conditions. All animal experiments and procedures were approved by the Garvan Institute of Medical Research/St Vincent's Hospital Animal Ethics Committee. Male and female mice were randomly assigned to treatment groups once tumors were established. C57BL/6 mice (RRID:MGI:5656552) were obtained from Australian BioResources (Moss Vale, NSW). Kaede mice (RRID:IMSR_RBRC05737) (65) were a gift from Professor Michio Tomura and were maintained on C57BL/6 background. Ly6GCre-tdTomato (C57BL/6-*Ly6g* (tm2621(Cre-tdTomato)Arte) neutrophil-specific reporter mice (36) were a gift from Professor Matthias Gunzer and crossed with B6.LSL td-Tomato (B6.Cg-*Gt(ROSA)26Sor*$^{tm14(CAG-tdTomato)Hze}$/J (IMSR Cat# JAX:007914 RRID:IMSR_JAX:007914) to generate BigRed/Catchup$^{IVM-red}$ mice and crossed to Albino.B6 or C57BL/6 mice with spontaneous mutations in the tyrosinase gene (B6(Cg)-*Tyr*$^{c-2J}$/J) for imaging. Lysozyme M fluorescent reporter mice were generated by crossing Lysozyme M Cre mice (Jackson Laboratory Cat#004781 RRID:IMSR_JAX:004781) to ROSA$^{mT/mG}$ mice (Jackson Laboratory Cat# 007576 RRID:IMSR_JAX:007576).

Tumor cell lines

Mouse Lewis Lung Carcinoma (LLC) (ATCC Cat# CRL-1642, RRID:CVCL_4358) cell line was purchased from ATCC (RRID:SCR_001672). LLC-eGFP cell line was a gift from Professor Robert Brink. B16F10-3C melanoma cell line (66) was a gift from Professor Wolfgang Weninger. Murine AT-3 mammary carcinoma (RRID:CVCL VR89) cell line was a gift from Dr Scott Abrams. KPC primary PDAC cell line (RRID:CVCL_XD11) (67) was a gift from Professor Paul Timpson.

Microbial bioparticles and microbes

S. aureus bioparticles (Wood strain without protein A) (Thermo Fisher Scientific Cat# S2859) were resuspended in PBS with 2 mM sodium azide and 4–20×10^6 bioparticles were injected directly into tumors. *Mycobacterium bovis* Bacillus Calmette Guerin were prepared as described previously (68).

Neutrophil recruitment into tumors

LLC cells were inoculated into ear pinnae of Kaede mice. When tumors reached 4-8 mm^3, they were photoconverted for 20 minutes with a violet light from a cold-light source fitted with a filter (Zeiss) to minimize thermal and phototoxicity (26,34) and immediately injected with 20×10^6 *S. aureus* bioparticles. Twenty-four, 48 and 72 h later mice were sacrificed and cell suspensions were analyzed by flow cytometry.

Microbial control of tumor growth

1-2 x 10^5 LLC, B16F10-3C, AT-3 or KPC tumor cells (in 5µl volume) were inoculated into ear pinnae of C57BL/6 mice. Once tumors were detected, they were treated with 4 – 20×10^6 *S. aureus* bioparticles or 5×10^6 CFU BCG or relevant vehicle control administered intratumorally every 2 days unless otherwise specified. Tumor dimensions were measured using calipers and volume calculated with the modified ellipsoidal formula V = ½ (Length × $Width^2$).

Neutrophil depletion

LLC tumors were grown in the ear pinnae of C57BL/6 mice. Once tumors became visible, neutrophils were depleted by intraperitoneal injection of 500 µg anti-Ly6G clone 1A8 (Bio X Cell Cat# BE0075-1, RRID:AB_1107721) or rat IgG2a isotype control clone 2A3 (Bio X Cell Cat# BE0089, RRID:AB_1107769). Twenty-four hours later 4-10×10^6 *S. aureus* bioparticles were injected into LLC tumors. The mice then had alternating days of maintenance dose of 250 µg anti-Ly6G/isotype i.p. and *S. aureus* bioparticles injected into tumors every 2 days. A total of 4 doses of 250 µg anti-Ly6G or isotype was administered whilst *S. aureus* bioparticles were given until mice reached ethical endpoints.

Neutrophil depletion in mice treated with anti-Ly6G was confirmed by flow cytometry. Red cells in blood samples were lysed with 10 mM $KHCO_3$, 0.1 mM EDTA and 166 mM NH_4Cl solution and then blocked with 5% normal mouse serum and then stained with unlabeled rat anti-mouse-Ly6G clone 1A8 (Bio X Cell Cat# BE0075-1, RRID:AB_1107721) primary antibody, washed and then stained with a secondary goat anti-rat IgG DyLight 649 (BioLegend Cat# 405411, RRID:AB_1575141) antibody and then washed with FACS buffer and blocked with 5% normal rat serum. Samples were washed again and then stained with labeled cell surface antibodies including CD11b-APCef780 clone M1/70 (Thermo Fisher Scientific Cat# 47-0112-80, RRID:AB_1603195).

CD8 T cell depletion

1 x 10^5 LLC tumor cells were inoculated into ear pinnae of C57BL/6 mice. Once tumors were visible, CD8 T cells were depleted by intraperitoneal injection of 250 µg anti-mouse CD8 clone 53-6.7 (Bio X cell Cat# BE0004-1 RRID:AB_1107671) or isotype clone IgG2a (Bio X cell Cat# BE0089 RRID:AB_1107769). Twenty-four hours later, 20 × 10^6 *S. aureus* bioparticles or vehicle control, were injected into tumors. Subsequent anti-CD8 antibodies were administered every 3 days and *S. aureus* bioparticles (or vehicle control) every 2 days. A total of five anti-CD8 or isotype injections were administered and *S. aureus* bioparticles (or vehicle) were given until mice reached ethical endpoints.

Neutrophil tumor cell killing assay

Twenty-four hours prior to start of assay 1.25 x 10^3 LLC-GFP cells were seeded in 24 well plates. Neutrophils were purified from bone marrow of C57BL/6 mice using the EasySep Mouse Neutrophil Enrichment Kit (Stemcell Technologies Cat# 19762) according to manufacturer's protocol. A ratio of 1 LLC-GFP to 3.4 purified neutrophils and/or 20 × 10^6 *S. aureus* bioparticles were added to each well and incubated for 24 hours in plain DMEM. Samples were prepared for flow cytometry and Sytox Blue (Thermo Fisher Scientific Cat# S34857) added prior to acquisition.

Effect of C5aR inhibition on microbial therapy

AT3 tumor cells (1x10^5 per mouse) were inoculated into ear pinnae of C57BL/6 mice. Once tumors were visible, 200μg/mouse of C5aR antagonist, PMX205 (69) (a gift from Trent Woodford) or vehicle control was injected i.p. daily. On alternative days 20 x 10^6 of *S. aureus* bioparticles or vehicle control were injected into tumors and tumor growth was measured.

Effect of ROS inhibition on microbial therapy

1x10^5 AT3 tumor cells were inoculated into ear pinnae of C57BL/6 mice. Tumor bearing mice received 500 μg/mouse of N-Acetylcysteine (NAC, Sigma-Aldrich Cat#A9165 CAS 616-91-1) or vehicle control daily i.p. from the time of tumor inoculation. Tumors were treated with 20 x 10^6 *S. aureus* bioparticles or vehicle control every second day once tumors were visible and tumor growth was measured.

Microbial and checkpoint inhibitor combination therapy

1 x 10^5 AT-3 tumor cells were inoculated into ear pinnae of C57BL/6 mice. Once tumors were detected, mice were treated with 2.5mg anti-mouse PD-1 (clone: RMP1-14 Bio X cell, Cat# BE0146, RRID: AB10949053)) and 1mg anti-mouse CTLA4 (Bio X cell, Cat# BE0131, RRID: AB10950184) or isotype control antibodies (clones: 2A3 Bio X Cell Cat# BE0089, RRID:AB_1107769, polyclonal Syrian hamster IgG Bio X cell, Cat#BE0087, RRID: AB1107782) via i.p. injection every three days for a total of five injections. The day after the first antibody injection, some mice were treated with 20×10^6 *S. aureus* bioparticles administered intratumorally every 3 days (a total of 3 injections) or vehicle control. Tumor growth was measured as previously.

Tumor recurrence model

C57BL/6 mice that were injected with AT-3 tumors and treated with microbial therapy every 2nd day were rested for at least 60 days after tumor resolution to confirm complete recovery. These mice and naïve C57BL/6 mice were challenged with 1 x 10^5 AT-3 tumor cells were inoculated into ear pinnae. Tumor growth was measured as previously.

Flow cytometry and antibodies

Single cell suspensions were made from tumors and lymph nodes by mechanical disruption and passed through 100 μM strainers. For blood samples red cells were lysed as previously. Staining for flow cytometry was performed in 96 well plates. Cells were blocked with CD16/CD32 clone 93 (Thermo Fisher Scientific Cat# 14-0161-86, RRID: AB_467135) for 15 min and stained with surface antibodies on ice in FACS buffer (1× PBS + 0.2% BSA and 0.1% NaN3 + 2 mM EDTA) for 30 min in the dark.

Cells for intracellular cytoplasmic staining were fixed with IC Fixation Buffer (Thermofisher Cat# 88-8824-00) for 30 min following surface staining. Samples were washed twice in Permeabilization Buffer (Thermofisher Cat# 88-8824-00) and stained in the same buffer with intracellular antibodies for 30 min at room temperature. Cells were washed twice in Permeabilization Buffer and resuspended in FACS buffer prior to flow cytometric acquisition. All samples were acquired on LSRII flow cytometer (BD Bioscience RRID:SCR_002159). Data was analyzed using FlowJo (FlowJo, RRID:SCR_008520).

Table 1. Antibodies used

Antibody	Source	Identifier
C1q biotin clone JL-1	Thermo Fisher Scientific	Thermo Fisher Scientific Cat# MA1-40312, RRID:AB_2067274
CD3ε Biotin clone 145-2C11	BD Biosciences	BD Biosciences Cat# 553060, RRID:AB_394593
CD3ε BV711 clone 145-2C11	BD Biosciences	BD Biosciences Cat# 563123, RRID:AB_2687954
CD3ε BUV395 clone 145-2C11	BD Biosciences	BD Biosciences Cat# 563565, RRID:AB_2738278
CD3, clone SP7	Novus Biologicals	Novus Biologicals Cat# NB600-1441, RRID: AB_789102
CD4 BV480 clone RM4-5	BD Biosciences	BD Biosciences Cat# 565634, RRID:AB_2739312
CD4 BV786 clone GK1.5	BD Biosciences	BD Biosciences Cat# 563331, RRID:AB_2738140
CD4 PECy7 clone RM4-5	BD Biosciences	BD Biosciences Cat# 561099, RRID:AB_2034007
CD8α APCef780 clone 53-6.7	Thermo Fisher Scientific	Thermo Fisher Scientific Cat# 47-0081-82, RRID:AB_1272185

CD8α clone D4W2Z	Cell Signaling Technology	Cell Signaling Technology, Cat# 98941S, RRID:AB_2756376
CD107a BV711 clone 1D4B	BD Biosciences	BD Biosciences Cat# 564348, RRID:AB_2738761
CD11b APCef780 clone M1/70	Thermo Fisher Scientific	Thermo Fisher Scientific Cat# 47-0112-80, RRID:AB_1603195
CD11c BV421 clone HL3	BD Biosciences	BD Biosciences Cat# 562782, RRID:AB_2737789
CD11c eFluor450 clone N418	Thermo Fisher Scientific	Thermo Fisher Scientific Cat# 48-0114-82, RRID:AB_1548654
CD16/CD32 Purified clone 93	Thermo Fisher Scientific	Thermo Fisher Scientific Cat# 14-0161-85, RRID:AB_467134
CD206 BV711 clone C068C2	BioLegend	BioLegend Cat# 141727, RRID:AB_2565822
CD366 (TIM3) APC clone RMT3-23	Miltenyi Biotec	Miltenyi Biotec Cat# 130-102-366, RRID:AB_2654180
CD44 BUV737 clone IM7	BD Biosciences	BD Biosciences Cat# 564392, RRID:AB_2738785
CD45 BV510 clone 30-F11	BD Biosciences	BD Biosciences Cat# 563891, RRID:AB_2734134
CD45 PE Cy7 clone 30-F11	BioLegend	BioLegend Cat# 139321, RRID:AB_312979
CD45 clone I3/2.3	Abcam	Abcam Cat# ab25386, RRID:AB_470499
CD45.2 FITC clone 104	BD Biosciences	BD Biosciences Cat# 553772, RRID:AB_395041
CD45.2 BUV395 clone 104	BD Biosciences	BD Biosciences Cat# 564616, RRID:AB_2738867
CD45R/B220 FITC clone RA3-6B2	BD Biosciences	BD Biosciences Cat# 553088, RRID:AB_394618
CD62L BV510 clone MEL-14	BD Biosciences	BD Biosciences Cat# 563117, RRID:AB_2738013
CD62L PerCP Cy5.5 clone MEL-14	Thermo Fisher Scientific	Thermo Fisher Scientific Cat# 45-0621-82, RRID:AB_996667
CD64 AF647 clone X54-5/7.1	BioLegend	BioLegend Cat# 139321, RRID:AB_2566560
CD64 BV786 clone X54-5/7.1	BD Biosciences	BD Biosciences Cat# 741024, RRID:AB_2740644
CD69 BV421 clone H1.2F3	BD Biosciences	BD Biosciences Cat# 562920, RRID:AB_2687478
CXCR2 APC clone 242216	R and D Systems	R and D Systems Cat# FAB2164A, RRID:AB_357124
CXCR4 Biotin clone 2B11	BD Biosciences	BD Biosciences Cat# 551958
F4/80 PE-CF594 clone T45-2342	BD Biosciences	BD Biosciences Cat# 565613, RRID:AB_2734770
GR-1 PerCP Cy5.5 clone RB6-8C5	BD Biosciences	BD Biosciences Cat# 552093, RRID:AB_394334
Granzyme B AF647 clone GB11	BioLegend	BioLegend Cat# 515405, RRID:AB_2294995

Histone H3 citrulline (R2 + R8 + R17) polyclonal	Abcam	Abcam Cat# ab5103, RRID:AB_304752
IFN-γ PECy7 clone XMG1.2	BD Biosciences	BD Biosciences Cat# 561040, RRID:AB_2034014
Rabbit Anti-Rat IgG Antibody, mouse adsorbed (H+L), Biotinylated	Vector Laboratories	Vector Laboratories Cat# BA-4001, RRID:AB_10015300

Two-photon intravital microscopy

To visualize tumor neutrophils LLC cells were inoculated into the ear pinnae of BigRed/Catchup^{IVMred} mice. Tumors were imaged ~10-14 days later. For some tumors, *S. aureus* 20×10^6 bioparticles were injected into tumors, which were imaged using two-photon microscopy 4 – 24 h later. LLC-eGFP cells were used to visualize interactions between neutrophils and tumor cells.

Intravital two-photon microscopy was based on a previously described method (70). Two-photon imaging was performed using an upright Zeiss 7MP two-photon microscope (Carl Zeiss) with a W Plan-Apochromat 20×/1.0 DIC (UV) Vis-IR water immersion objective. Four external non-descanned detectors were used to detect blue (SP 485), green (BP 500-550), red (BP 565-610) and far red (BP 640-710). High repetition rate femtosecond pulsed excitation was provided by a Chameleon Vision II Ti:Sa laser (Coherent Scientific) with 690-1064nm tuning range. We acquired 3µm z-steps at 512×512 pixels and resolution 0.83µm/pixel at a frame rate of 10 fps and dwell time of 1.27 µs/pixel using bidirectional scanning. Anesthesia was induced with 100mg/kg ketamine/5mg/kg xylazine and maintained with 1-2% isoflurane supplemented with 100% oxygen at a flow rate of 500ml/min via a nose cone. Anesthetized mice were kept warm using a customized heated SmartStage (Biotherm). The ear was immobilized on a base of thermal conductive T-putty (Thermagon Inc.) using Vetbond tissue adhesive (3M).

Adoptive transfer of bone marrow cells

For the single adoptive transfer, bone marrow was harvested by flushing the femurs of BigRed/Catchup$^{IVM\text{-}red}$ mice using cold PBS. Erythrocytes were removed by lysing with 10 mM $KHCO_3$, 0.1 mM EDTA and 166 mM NH_4Cl and washing twice with PBS. The resulting cell suspension was transferred intravenously into recipient C57BL/6 mice bearing LLC tumors.

For the double adoptive transfer, bone marrow from the first donor mouse strain (Lysozyme M tdTomato) was harvested as described above and transferred intravenously into recipient C57BL/6 mice bearing LLC tumors. One day later, bone marrow from the second donor mouse strain (lysozyme M Kikume) was harvested as described above and transferred intravenously into the same

recipient. Tumors were imaged 2h later using intravital two-photon microscopy, and again at 24 h after the second adoptive transfer.

Image processing and data analysis

Raw image files were processed using Imaris (Imaris, RRID:SCR_007370) software. A Gaussian filter was applied to reduce background noise. Tracking was performed using Imaris spot detection function to locate the centroid of cells. Motility parameters such as cell displacement (or track length calculated as the total length of displacements within the track) and track speed (calculated by dividing track length by time) were obtained using Imaris Statistics function. All modelling and statistical analysis was performed in GraphPad Prism (GraphPad Prism, RRID:SCR_002798).

To quantitate LLC-eGFP cells, Imaris spot detection function was used to identify eGFP cells in the green channel for image areas of 250×250 μm in untreated and bioparticle treated tumors. The number of LLC cells remaining in each area was then calculated and recorded.

Whole tumor section microscopy

Tumors were harvested from BigRed/Catchup$^{IVM\text{-}red}$ mice and fixed for 45-90 min in the dark at room temperature in fixing buffer (1×PBS, 4% Formalin and 10% Sucrose). Subsequently, tumors were sequentially incubated with 10%, 20% and 30% Sucrose in PBS for 8 h in the dark at 4°C, embedded in O.C.T. compound (Sakura Finetek) and frozen at -80 °C. One hundred μm-thick cryosections of LLC tumor were cut and imaged using two-photon microscopy**.** Acquired images were processed and analyzed using Imaris software.

Immunohistochemistry

Tumors were placed into 10% neutral-buffered formalin, processed and embedded into paraffin wax. Immunohistochemistry (IHC) was performed on the Leica Bond RX platform by the Garvan Institute of Medical Research Histopathology Facility. Four micrometer-thick sections were collected onto positively-charged glass slides and baked for 2 h at 60C. Following routine deparaffinization, antigen retrieval, washing and blocking, primary antibodies were diluted and applied to the slides. The dilutions used were: 1:150 for anti-CD45 I3/2.3 (Abcam Cat# ab25386, RRID:AB_470499), 1:150 for anti-CD8α clone D4W2Z (Cell Signaling Technology Cat# 98941S, RRID:AB_2756376), 1:4000 for anti-Ly6G clone 1A8 (Bio X Cell Cat# BE0075-1, RRID:AB_1107721), 1:50 for anti-C1q clone JL-1 (Thermo Fisher Scientific Cat# MA1-40312, RRID:AB_2067274), 1:1000 for anti-histone H3 (citrulline R2 + R8 + R17) polyclonal (Abcam Cat# ab5103, RRID:AB_304752) and 1:200 for anti-neutrophil elastase FITC polyclonal (Biorbyt Cat# orb3644). Following incubation, primary antibodies were aspirated and slides were washed. Rabbit primary antibodies were detected using Bond Polymer Refine Detection kit (Leica Cat#DS9800). Rat primary antibodies were detected using

Bond Polymer Refine Detection kit (Leica Cat#DS9800) with biotinylated rabbit anti-rat IgG secondary antibody (Vector Laboratories Cat# BA-4001, RRID:AB_10015300)). Sections were then counterstained with hematoxylin and cover-slipped. Slides were imaged at 40x using the Nanozoomer S210 digital slide scanner (Hamamatsu) and analyzed using QuPath (RRID:SCR_018257) (71).

scRNAseq analysis of tumor neutrophils

AT-3 tumor cells were injected into ear pinnae of 8 weeks old C57BL/6 female and male mice ($0.3x10^6$ cells in 5µl PBS). Ten days after tumor cell inoculation, mice were divided into 3 groups and either left untreated or were treated with 20×10^6 *S. aureus* bioparticles or saline vehicle administered intratumorally, and sacrificed 24 hours later. Tumors were dissected, placed in 2 ml PBS+ 2%BSA and gently disaggregated through a 100 µm cell strainer using a 1ml syringe plunger. Cells were collected, centrifuged and resuspended in 5ml PBS+ 2%BSA. Single-cell suspensions were stained for 30 min at 4 °C with Zombie UV™ Fixable Viability kit (Biolegend cat#423107), washed and resuspended in 50ul PBS+1%FBS with fluorophore-conjugated antibodies (FITC-conjugated anti-Ly6G, PeCy7-conjugated anti-CD45, APCCy7-conjugated-anti-CD11b), stained again for 30 min at 4 °C, filtered through 100 µm cell strainers, and sorted using a BD FACSymphony cell sorter (BD Biosciences) into PBS/2% BSA. Single-cell sequencing was conducted at the UTS Single Cell Technology Facility using the BD Rhapsody instrument. The cell preparation time before loading onto the BD Rhapsody was <3 h. Cell viability and counting were evaluated with the BD Rhapsody™ Scanner following a standard protocol provided by the manufacturer (BD Biosciences), and samples with viabilities >75% were used for sequencing. Libraries were constructed using the BD Rhapsody WTA Amp Kit (BD Biosciences, cat# 633801). Once prepared, indexed complementary DNA (cDNA) libraries were sequenced with NovaSeq 6000 S1 100 cycle flowcell with 1% Illumina PhiX Control v3 spike-in by Ramaciotti Centre for Genomics.

scRNA-seq data processing

The BD Rhapsody WTA Analysis Pipeline was used to align the sequencing reads (fastq) to the GRCm38 mouse genome (M19 transcriptome) and quantify gene expression in each cell. A gene expression matrix was generated for each sample quantifying the number of unique molecular identifiers (UMIs) for each gene per cell. This gene expression matrix was load into python (v3.7) and preprocessed using scanpy (v1.9.1, (72)). Doublets in each sample were identified and removed using scrublet (v0.2.3, (73)). Per cell quality control (QC) statistics, including library size measured as the total UMIs, number of genes, the percent of reads in the top 50 genes and percent of reads aligned to genes on the mitochondrial genome (mitochondrial content) were computed using the *scanpy.pp.calculate_qc_metrics* function. Cells were filtered based on library size to those with 2,000 - 40,000 UMI and mitochondrial content <15%. Genes were filtered to those detected in more than

eight cells. After this QC 16850 cells remained, comprised of 3895, 5226 and 7729 cells from the resting, control and stimulated conditions respectively. Data were normalized to 10000 reads per cell and log transformed for downstream analysis. Counts were smoothed for visualization in heatmaps and UMAP plots using MAGIC (v2.0.3, (74)). MAGIC smoothed counts were not used for any statistical analysis.

Single cell graph construction, community detection and marker identification

Genes with highly variable expression (HVGs) were determined within each condition, and the union of HVGs from each condition (6594 genes) was used to model the biological variation across the experiment. The dimensionality of data was reduced to the top 100 principle components and these were used to construct a nearest neighbor graph of cells with the *scanpy.pp.neighbors* function (n_neighbours=15). A batch corrected graph was also generated from principle components adjusted to correct for sample condition using Harmony (harmonypy v0.0.4, (75)). This analysis was performed to determine whether batch effect between conditions was driving the separation of neutrophil states. As the batch corrected embedding did not show substantial change in the integration between conditions, the original nearest neighbor graph of cells was used for all downstream analysis.

Highly connected communities of cells in this graph were detected using the Leiden algorithm (resolution=1, (76)), identifying 18 clusters of cells with a median of 717 cells (Min:41, Max:2481). Data were exported from Python and downstream analysis performed in R (v4.0.2, R Core Team (2022). R: A language and environment for statistical computing. R Foundation for Statistical Computing, Vienna, Austria. URL https://www.R-project.org/.) and visualized using ggplot2 (v3.3.5, H. Wickham. ggplot2: Elegant Graphics for Data Analysis. Springer-Verlag New York, 2016.). Markers for each cluster were identified using the *FindMarkers* function from the Seurat R-package (v3.2.2, (77)).

Cell type assignment and gene-set enrichment

Cell-types were assigned based in the enrichment of established cell-type markers among cluster markers (LFC > 0.25). Markers of cell types associated with 'Connective tissue', 'Smooth muscle', 'Immune system', 'Vasculature', 'Blood' or 'Epithelium' in the PanglaoDB database (v27/03/2020, (78)) were tested for enrichment with a 1-sided Fisher's exact test using the clusterProfiler R-package (v3.16.1, (79)). P-values were false discovery rate (FDR) adjusted prior to determining significance. Seven cell-types were identified among the 18 clusters, with multiple clusters per cell type, including five distinct Neutrophil clusters (denoted Neu1-5). Gene ontology biological processes (GOBP) over represented among markers (LFC > 1) for each Neutrophil cluster were determined by 1-sided Fisher's exact test using clusterProfiler and FDR adjusted p-values (80). Redundant GOBP terms were removed based on the Wang measure of semantic similarity (>0.9 similarity score) (81) using

the rrvgo R-package (v1.0.2, Sayols S (2020). rrvgo: a Bioconductor package to reduce and visualize Gene Ontology terms.). Neutrophil Maturation was scored using a previously defined geneset from ((55)) using the *AddModuleScore* function from the Seurat R-package (v3.2.2, (77)).

Statistical analysis

The statistical distribution of experimental data was determined using a D'Agostino-Pearson omnibus normality test. The statistical significance of experimental data for comparisons of two groups was determined using either an unpaired T-test when distribution was normal and unpaired Mann-Whitney test if distribution was not normal. Statistical significance, for comparison of three or more groups unmatched ordinary one-way ANOVA test when distribution was normal and unmatched Kruskal-Wallis test if distribution was not normal. All analysis was done on GraphPad Prism (GraphPad Prism, RRID:SCR_002798).

REFERENCES

1. Shalapour S, Karin M. Pas de Deux: Control of Anti-tumor Immunity by Cancer-Associated Inflammation. Immunity **2019**;51(1):15-26 doi 10.1016/j.immuni.2019.06.021.
2. Hoption Cann SA, van Netten JP, van Netten C. Dr William Coley and tumour regression: a place in history or in the future. Postgrad Med J **2003**;79(938):672-80.
3. Pettenati C, Ingersoll MA. Mechanisms of BCG immunotherapy and its outlook for bladder cancer. Nat Rev Urol **2018**;15(10):615-25 doi 10.1038/s41585-018-0055-4.
4. Grivennikov SI, Greten FR, Karin M. Immunity, inflammation, and cancer. Cell **2010**;140(6):883-99 doi 10.1016/j.cell.2010.01.025.
5. Urban-Wojciuk Z, Khan MM, Oyler BL, Fahraeus R, Marek-Trzonkowska N, Nita-Lazar A*, et al.* The Role of TLRs in Anti-cancer Immunity and Tumor Rejection. Front Immunol **2019**;10:2388 doi 10.3389/fimmu.2019.02388.
6. Suttmann H, Riemensberger J, Bentien G, Schmaltz D, Stockle M, Jocham D*, et al.* Neutrophil granulocytes are required for effective Bacillus Calmette-Guerin immunotherapy of bladder cancer and orchestrate local immune responses. Cancer Res **2006**;66(16):8250-7 doi 10.1158/0008-5472.CAN-06-1416.
7. Kubes P. The enigmatic neutrophil: what we do not know. Cell Tissue Res **2018**;371(3):399-406 doi 10.1007/s00441-018-2790-5.
8. Coffelt SB, Wellenstein MD, de Visser KE. Neutrophils in cancer: neutral no more. Nat Rev Cancer **2016**;16(7):431-46 doi 10.1038/nrc.2016.52.
9. Nozawa H, Chiu C, Hanahan D. Infiltrating neutrophils mediate the initial angiogenic switch in a mouse model of multistage carcinogenesis. Proc Natl Acad Sci U S A **2006**;103(33):12493-8 doi 10.1073/pnas.0601807103.
10. Schmielau J, Finn OJ. Activated granulocytes and granulocyte-derived hydrogen peroxide are the underlying mechanism of suppression of t-cell function in advanced cancer patients. Cancer Res **2001**;61(12):4756-60.
11. Rice CM, Davies LC, Subleski JJ, Maio N, Gonzalez-Cotto M, Andrews C*, et al.* Tumour-elicited neutrophils engage mitochondrial metabolism to circumvent nutrient limitations and maintain immune suppression. Nat Commun **2018**;9(1):5099 doi 10.1038/s41467-018-07505-2.
12. Xu W, Dong J, Zheng Y, Zhou J, Yuan Y, Ta HM*, et al.* Immune-Checkpoint Protein VISTA Regulates Antitumor Immunity by Controlling Myeloid Cell-Mediated

Inflammation and Immunosuppression. Cancer Immunol Res **2019**;7(9):1497-510 doi 10.1158/2326-6066.CIR-18-0489.
13. Bald T, Quast T, Landsberg J, Rogava M, Glodde N, Lopez-Ramos D*, et al.* Ultraviolet-radiation-induced inflammation promotes angiotropism and metastasis in melanoma. Nature **2014**;507(7490):109-13 doi 10.1038/nature13111.
14. Park J, Wysocki RW, Amoozgar Z, Maiorino L, Fein MR, Jorns J*, et al.* Cancer cells induce metastasis-supporting neutrophil extracellular DNA traps. Sci Transl Med **2016**;8(361):361ra138 doi 10.1126/scitranslmed.aag1711.
15. Dart A. Metastasis: CXCR2-targeted therapy for pancreatic cancer. Nat Rev Cancer **2016**;16(7):411 doi 10.1038/nrc.2016.67.
16. Glodde N, Bald T, van den Boorn-Konijnenberg D, Nakamura K, O'Donnell JS, Szczepanski S*, et al.* Reactive Neutrophil Responses Dependent on the Receptor Tyrosine Kinase c-MET Limit Cancer Immunotherapy. Immunity **2017**;47(4):789-802 e9 doi 10.1016/j.immuni.2017.09.012.
17. Highfill SL, Cui Y, Giles AJ, Smith JP, Zhang H, Morse E*, et al.* Disruption of CXCR2-mediated MDSC tumor trafficking enhances anti-PD1 efficacy. Sci Transl Med **2014**;6(237):237ra67 doi 10.1126/scitranslmed.3007974.
18. Steele CW, Karim SA, Leach JDG, Bailey P, Upstill-Goddard R, Rishi L*, et al.* CXCR2 Inhibition Profoundly Suppresses Metastases and Augments Immunotherapy in Pancreatic Ductal Adenocarcinoma. Cancer Cell **2016**;29(6):832-45 doi 10.1016/j.ccell.2016.04.014.
19. Faget J, Groeneveld S, Boivin G, Sankar M, Zangger N, Garcia M*, et al.* Neutrophils and Snail Orchestrate the Establishment of a Pro-tumor Microenvironment in Lung Cancer. Cell Rep **2017**;21(11):3190-204 doi 10.1016/j.celrep.2017.11.052.
20. Blaisdell A, Crequer A, Columbus D, Daikoku T, Mittal K, Dey SK*, et al.* Neutrophils Oppose Uterine Epithelial Carcinogenesis via Debridement of Hypoxic Tumor Cells. Cancer Cell **2015**;28(6):785-99 doi 10.1016/j.ccell.2015.11.005.
21. Finisguerra V, Di Conza G, Di Matteo M, Serneels J, Costa S, Thompson AA*, et al.* MET is required for the recruitment of anti-tumoural neutrophils. Nature **2015**;522(7556):349-53 doi 10.1038/nature14407.
22. Granot Z, Henke E, Comen EA, King TA, Norton L, Benezra R. Tumor entrained neutrophils inhibit seeding in the premetastatic lung. Cancer Cell **2011**;20(3):300-14 doi 10.1016/j.ccr.2011.08.012.
23. Stoppacciaro A, Melani C, Parenza M, Mastracchio A, Bassi C, Baroni C*, et al.* Regression of an established tumor genetically modified to release granulocyte colony-stimulating factor requires granulocyte-T cell cooperation and T cell-produced interferon gamma. J Exp Med **1993**;178(1):151-61 doi 10.1084/jem.178.1.151.
24. Colombo MP, Ferrari G, Stoppacciaro A, Parenza M, Rodolfo M, Mavilio F*, et al.* Granulocyte colony-stimulating factor gene transfer suppresses tumorigenicity of a murine adenocarcinoma in vivo. J Exp Med **1991**;173(4):889-97 doi 10.1084/jem.173.4.889.
25. Fridlender ZG, Sun J, Kim S, Kapoor V, Cheng G, Ling L*, et al.* Polarization of tumor-associated neutrophil phenotype by TGF-beta: "N1" versus "N2" TAN. Cancer Cell **2009**;16(3):183-94 doi 10.1016/j.ccr.2009.06.017.
26. Torcellan T, Hampton HR, Bailey J, Tomura M, Brink R, Chtanova T. In vivo photolabeling of tumor-infiltrating cells reveals highly regulated egress of T-cell subsets from tumors. Proc Natl Acad Sci U S A **2017**;114(22):5677-82 doi 10.1073/pnas.1618446114.
27. Mixter PF, Russell JQ, Morrissette GJ, Charland C, Aleman-Hoey D, Budd RC. A model for the origin of TCR-alphabeta+ CD4-CD8- B220+ cells based on high affinity TCR signals. J Immunol **1999**;162(10):5747-56.
28. Limkar AR, Mai E, Sek AC, Percopo CM, Rosenberg HF. Frontline Science: Cytokine-mediated developmental phenotype of mouse eosinophils: IL-5-associated expression of the Ly6G/Gr1 surface Ag. J Leukoc Biol **2020**;107(3):367-77 doi 10.1002/JLB.1HI1019-116RR.

29. Temiz MZ, Colakerol A, Ulus I, Kilic E, Paslanmaz F, Sahin S*, et al.* Prediction of non-muscle-invasive bladder cancer recurrence during intravesical BCG immunotherapy by use of peripheral blood eosinophil count and percentage: a preliminary report. Cancer Immunol Immunother **2021**;70(1):245-52 doi 10.1007/s00262-020-02673-x.
30. Evrard M, Kwok IWH, Chong SZ, Teng KWW, Becht E, Chen J*, et al.* Developmental Analysis of Bone Marrow Neutrophils Reveals Populations Specialized in Expansion, Trafficking, and Effector Functions. Immunity **2018**;48(2):364-79 e8 doi 10.1016/j.immuni.2018.02.002.
31. Amulic B, Cazalet C, Hayes GL, Metzler KD, Zychlinsky A. Neutrophil function: from mechanisms to disease. Annu Rev Immunol **2012**;30:459-89 doi 10.1146/annurev-immunol-020711-074942.
32. Grieshaber-Bouyer R, Nigrovic PA. Neutrophil Heterogeneity as Therapeutic Opportunity in Immune-Mediated Disease. Front Immunol **2019**;10:346 doi 10.3389/fimmu.2019.00346.
33. Silvestre-Roig C, Hidalgo A, Soehnlein O. Neutrophil heterogeneity: implications for homeostasis and pathogenesis. Blood **2016**;127(18):2173-81 doi 10.1182/blood-2016-01-688887.
34. Hampton HR, Bailey J, Tomura M, Brink R, Chtanova T. Microbe-dependent lymphatic migration of neutrophils modulates lymphocyte proliferation in lymph nodes. Nat Commun **2015**;6:7139 doi 10.1038/ncomms8139.
35. Wheeler MA, Smith SD, Garcia-Cardena G, Nathan CF, Weiss RM, Sessa WC. Bacterial infection induces nitric oxide synthase in human neutrophils. J Clin Invest **1997**;99(1):110-6 doi 10.1172/JCI119121.
36. Hasenberg A, Hasenberg M, Mann L, Neumann F, Borkenstein L, Stecher M*, et al.* Catchup: a mouse model for imaging-based tracking and modulation of neutrophil granulocytes. Nat Methods **2015**;12(5):445-52 doi 10.1038/nmeth.3322.
37. Chtanova T, Schaeffer M, Han SJ, van Dooren GG, Nollmann M, Herzmark P*, et al.* Dynamics of neutrophil migration in lymph nodes during infection. Immunity **2008**;29(3):487-96 doi 10.1016/j.immuni.2008.07.012.
38. Lammermann T, Afonso PV, Angermann BR, Wang JM, Kastenmuller W, Parent CA*, et al.* Neutrophil swarms require LTB4 and integrins at sites of cell death in vivo. Nature **2013**;498(7454):371-5 doi 10.1038/nature12175.
39. Quail DF, Amulic B, Aziz M, Barnes BJ, Eruslanov E, Fridlender ZG*, et al.* Neutrophil phenotypes and functions in cancer: A consensus statement. J Exp Med **2022**;219(6) doi 10.1084/jem.20220011.
40. Lewis HD, Liddle J, Coote JE, Atkinson SJ, Barker MD, Bax BD*, et al.* Inhibition of PAD4 activity is sufficient to disrupt mouse and human NET formation. Nat Chem Biol **2015**;11(3):189-91 doi 10.1038/nchembio.1735.
41. Martin C, Burdon PC, Bridger G, Gutierrez-Ramos JC, Williams TJ, Rankin SM. Chemokines acting via CXCR2 and CXCR4 control the release of neutrophils from the bone marrow and their return following senescence. Immunity **2003**;19(4):583-93 doi 10.1016/s1074-7613(03)00263-2.
42. Devi S, Wang Y, Chew WK, Lima R, N AG, Mattar CN*, et al.* Neutrophil mobilization via plerixafor-mediated CXCR4 inhibition arises from lung demargination and blockade of neutrophil homing to the bone marrow. J Exp Med **2013**;210(11):2321-36 doi 10.1084/jem.20130056.
43. Lord BI, Molineux G, Pojda Z, Souza LM, Mermod JJ, Dexter TM. Myeloid cell kinetics in mice treated with recombinant interleukin-3, granulocyte colony-stimulating factor (CSF), or granulocyte-macrophage CSF in vivo. Blood **1991**;77(10):2154-9.
44. Gatti-Mays ME, Balko JM, Gameiro SR, Bear HD, Prabhakaran S, Fukui J*, et al.* If we build it they will come: targeting the immune response to breast cancer. NPJ Breast Cancer **2019**;5:37 doi 10.1038/s41523-019-0133-7.

45. Bonaventura P, Shekarian T, Alcazer V, Valladeau-Guilemond J, Valsesia-Wittmann S, Amigorena S*, et al.* Cold Tumors: A Therapeutic Challenge for Immunotherapy. Front Immunol **2019**;10:168 doi 10.3389/fimmu.2019.00168.
46. Manji GA, Olive KP, Saenger YM, Oberstein P. Current and Emerging Therapies in Metastatic Pancreatic Cancer. Clin Cancer Res **2017**;23(7):1670-8 doi 10.1158/1078-0432.CCR-16-2319.
47. Boivin G, Faget J, Ancey PB, Gkasti A, Mussard J, Engblom C*, et al.* Durable and controlled depletion of neutrophils in mice. Nat Commun **2020**;11(1):2762 doi 10.1038/s41467-020-16596-9.
48. Le Gal K, Ibrahim MX, Wiel C, Sayin VI, Akula MK, Karlsson C*, et al.* Antioxidants can increase melanoma metastasis in mice. Sci Transl Med **2015**;7(308):308re8 doi 10.1126/scitranslmed.aad3740.
49. Sayin VI, Ibrahim MX, Larsson E, Nilsson JA, Lindahl P, Bergo MO. Antioxidants accelerate lung cancer progression in mice. Sci Transl Med **2014**;6(221):221ra15 doi 10.1126/scitranslmed.3007653.
50. Zhang VX, Sze KM, Chan LK, Ho DW, Tsui YM, Chiu YT*, et al.* Antioxidant supplements promote tumor formation and growth and confer drug resistance in hepatocellular carcinoma by reducing intracellular ROS and induction of TMBIM1. Cell Biosci **2021**;11(1):217 doi 10.1186/s13578-021-00731-0.
51. Matlung HL, Babes L, Zhao XW, van Houdt M, Treffers LW, van Rees DJ*, et al.* Neutrophils Kill Antibody-Opsonized Cancer Cells by Trogoptosis. Cell Rep **2018**;23(13):3946-59 e6 doi 10.1016/j.celrep.2018.05.082.
52. Pellas TC, Boyar W, van Oostrum J, Wasvary J, Fryer LR, Pastor G*, et al.* Novel C5a receptor antagonists regulate neutrophil functions in vitro and in vivo. J Immunol **1998**;160(11):5616-21.
53. Veglia F, Hashimoto A, Dweep H, Sanseviero E, De Leo A, Tcyganov E*, et al.* Analysis of classical neutrophils and polymorphonuclear myeloid-derived suppressor cells in cancer patients and tumor-bearing mice. J Exp Med **2021**;218(4) doi 10.1084/jem.20201803.
54. Monaco G, Lee B, Xu W, Mustafah S, Hwang YY, Carre C*, et al.* RNA-Seq Signatures Normalized by mRNA Abundance Allow Absolute Deconvolution of Human Immune Cell Types. Cell Rep **2019**;26(6):1627-40 e7 doi 10.1016/j.celrep.2019.01.041.
55. Xie X, Shi Q, Wu P, Zhang X, Kambara H, Su J*, et al.* Single-cell transcriptome profiling reveals neutrophil heterogeneity in homeostasis and infection. Nat Immunol **2020**;21(9):1119-33 doi 10.1038/s41590-020-0736-z.
56. Griffith JW, Sokol CL, Luster AD. Chemokines and chemokine receptors: positioning cells for host defense and immunity. Annu Rev Immunol **2014**;32:659-702 doi 10.1146/annurev-immunol-032713-120145.
57. Franciszkiewicz K, Boissonnas A, Boutet M, Combadiere C, Mami-Chouaib F. Role of chemokines and chemokine receptors in shaping the effector phase of the antitumor immune response. Cancer Res **2012**;72(24):6325-32 doi 10.1158/0008-5472.CAN-12-2027.
58. Li F, Du X, Lan F, Li N, Zhang C, Zhu C*, et al.* Eosinophilic inflammation promotes CCL6-dependent metastatic tumor growth. Sci Adv **2021**;7(22) doi 10.1126/sciadv.abb5943.
59. Peters NC, Egen JG, Secundino N, Debrabant A, Kimblin N, Kamhawi S*, et al.* In vivo imaging reveals an essential role for neutrophils in leishmaniasis transmitted by sand flies. Science **2008**;321(5891):970-4 doi 10.1126/science.1159194.
60. Yam AO, Chtanova T. Imaging the neutrophil: Intravital microscopy provides a dynamic view of neutrophil functions in host immunity. Cell Immunol **2019** doi 10.1016/j.cellimm.2019.01.003.
61. Ng LG, Qin JS, Roediger B, Wang Y, Jain R, Cavanagh LL*, et al.* Visualizing the neutrophil response to sterile tissue injury in mouse dermis reveals a three-phase cascade of events. J Invest Dermatol **2011**;131(10):2058-68 doi 10.1038/jid.2011.179.

62. Koya MP, Simon MA, Soloway MS. Complications of intravesical therapy for urothelial cancer of the bladder. J Urol **2006**;175(6):2004-10 doi 10.1016/S0022-5347(06)00264-3.
63. Smith M, Garcia-Martinez E, Pitter MR, Fucikova J, Spisek R, Zitvogel L*, et al.* Trial Watch: Toll-like receptor agonists in cancer immunotherapy. Oncoimmunology **2018**;7(12):e1526250 doi 10.1080/2162402X.2018.1526250.
64. Sagnella SM, Yang L, Stubbs GE, Boslem E, Martino-Echarri E, Smolarczyk K*, et al.* Cyto-Immuno-Therapy for Cancer: A Pathway Elicited by Tumor-Targeted, Cytotoxic Drug-Packaged Bacterially Derived Nanocells. Cancer Cell **2020**;37(3):354-70 e7 doi 10.1016/j.ccell.2020.02.001.
65. Tomura M, Yoshida N, Tanaka J, Karasawa S, Miwa Y, Miyawaki A*, et al.* Monitoring cellular movement in vivo with photoconvertible fluorescence protein "Kaede" transgenic mice. Proc Natl Acad Sci U S A **2008**;105(31):10871-6 doi 0802278105 [pii] 10.1073/pnas.0802278105.
66. Tikoo S, Jain R, Tomasetig F, On K, Martinez B, Heu C*, et al.* Amelanotic B16-F10 Melanoma Compatible with Advanced Three-Dimensional Imaging Modalities. J Invest Dermatol **2021**;141(8):2090-4 e6 doi 10.1016/j.jid.2021.01.025.
67. Morton JP, Karim SA, Graham K, Timpson P, Jamieson N, Athineos D*, et al.* Dasatinib inhibits the development of metastases in a mouse model of pancreatic ductal adenocarcinoma. Gastroenterology **2010**;139(1):292-303 doi 10.1053/j.gastro.2010.03.034.
68. Counoupas C, Pinto R, Nagalingam G, Britton WJ, Triccas JA. Protective efficacy of recombinant BCG over-expressing protective, stage-specific antigens of Mycobacterium tuberculosis. Vaccine **2018**;36(19):2619-29 doi 10.1016/j.vaccine.2018.03.066.
69. Kumar V, Lee JD, Clark RJ, Noakes PG, Taylor SM, Woodruff TM. Preclinical Pharmacokinetics of Complement C5a Receptor Antagonists PMX53 and PMX205 in Mice. ACS Omega **2020**;5(5):2345-54 doi 10.1021/acsomega.9b03735.
70. Chtanova T, Hampton HR, Waterhouse LA, Wood K, Tomura M, Miwa Y*, et al.* Real-time interactive two-photon photoconversion of recirculating lymphocytes for discontinuous cell tracking in live adult mice. Journal of biophotonics **2014**;7(6):425-33 doi 10.1002/jbio.201200175.
71. Bankhead P, Loughrey MB, Fernandez JA, Dombrowski Y, McArt DG, Dunne PD*, et al.* QuPath: Open source software for digital pathology image analysis. Sci Rep **2017**;7(1):16878 doi 10.1038/s41598-017-17204-5.
72. Wolf FA, Angerer P, Theis FJ. SCANPY: large-scale single-cell gene expression data analysis. Genome Biol **2018**;19(1):15 doi 10.1186/s13059-017-1382-0.
73. Wolock SL, Lopez R, Klein AM. Scrublet: Computational Identification of Cell Doublets in Single-Cell Transcriptomic Data. Cell Syst **2019**;8(4):281-91 e9 doi 10.1016/j.cels.2018.11.005.
74. van Dijk D, Sharma R, Nainys J, Yim K, Kathail P, Carr AJ*, et al.* Recovering Gene Interactions from Single-Cell Data Using Data Diffusion. Cell **2018**;174(3):716-29 e27 doi 10.1016/j.cell.2018.05.061.
75. Korsunsky I, Millard N, Fan J, Slowikowski K, Zhang F, Wei K*, et al.* Fast, sensitive and accurate integration of single-cell data with Harmony. Nat Methods **2019**;16(12):1289-96 doi 10.1038/s41592-019-0619-0.
76. Traag VA, Waltman L, van Eck NJ. From Louvain to Leiden: guaranteeing well-connected communities. Sci Rep **2019**;9(1):5233 doi 10.1038/s41598-019-41695-z.
77. Stuart T, Butler A, Hoffman P, Hafemeister C, Papalexi E, Mauck WM, 3rd*, et al.* Comprehensive Integration of Single-Cell Data. Cell **2019**;177(7):1888-902 e21 doi 10.1016/j.cell.2019.05.031.
78. Franzen O, Gan LM, Bjorkegren JLM. PanglaoDB: a web server for exploration of mouse and human single-cell RNA sequencing data. Database (Oxford) **2019**;2019 doi 10.1093/database/baz046.

79. Yu G, Wang LG, Han Y, He QY. clusterProfiler: an R package for comparing biological themes among gene clusters. OMICS **2012**;16(5):284-7 doi 10.1089/omi.2011.0118.
80. Ashburner M, Ball CA, Blake JA, Botstein D, Butler H, Cherry JM*, et al.* Gene ontology: tool for the unification of biology. The Gene Ontology Consortium. Nat Genet **2000**;25(1):25-9 doi 10.1038/75556.
81. Wang JZ, Du Z, Payattakool R, Yu PS, Chen CF. A new method to measure the semantic similarity of GO terms. Bioinformatics **2007**;23(10):1274-81 doi 10.1093/bioinformatics/btm087.

ACKNOWLEDGMENTS

Funding:

This research was supported by funding to T.C. from the National Breast Cancer Foundation (IIRS-22-053), UNSW Cellular Genomics Futures Institute, UNSW Sydney, Avner Grant from PanKind, The Australian Pancreatic Cancer Foundation. A.O.Y. is supported by Australian Government Research Training Program and Royal Australasian College of Physicians Fellows Research Entry Scholarships, a Phil Salter Immuno-Oncology Fellowship. Intravital microscopy centre supported by Peter and Val Duncan. S.E.Y and L.D.G. acknowledge funding from the Kinghorn Foundation. D.G.O. is a National Breast Cancer Foundation Elaine Henry Fellow (IIRS-21-096).

Author contributions:

Conceptualization: TC, AOY, STG
Methodology: AOY, JB, FL, JAT, MG, TB, DGO
Investigation: AOY, JB, FL, AJ, CC, SEY, LDG
Visualization: TC, JB, AOY, MG, SEY, LDG
Supervision: TC, JAT
Writing and editing: TC, AOY, STG, TB

Competing interests: Authors declare that they have no competing interests.

FIGURE LEGENDS

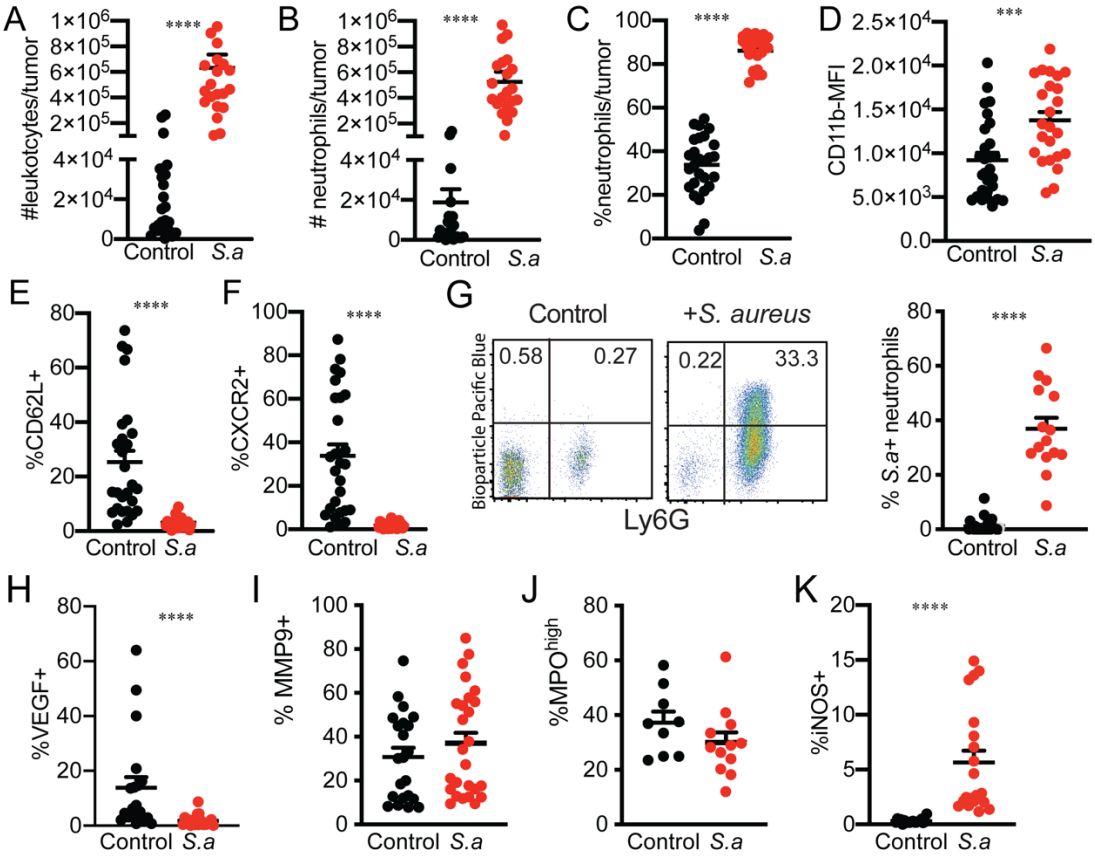

Figure 1. Microbe-driven recruitment and activation of intratumoral neutrophils. *S. aureus* bioparticle injection into tumors leads to an influx of leukocytes (A) and especially neutrophils (B) which made up the majority of tumor leukocytes after challenge (C). Neutrophil activation was assessed by expression of CD11b (D), CD62L (E) and CXCR2 (F) detected by flow cytometry 24 hours post S. aureus injection. G. Phagocytosis of labeled S. aureus bioparticles by intratumoral neutrophils. Representative flow cytometry plots (left) and pooled data (right) are shown. Proportion of VEGF- (H), iNOS (I), MMP9 (J) and MPO (K) expressing neutrophils was quantitated by flow cytometry in control and *S.aureus*-treated tumors. Mean + SEM from 3-5 (A-J) and 2 (K) independent experiments. Each circle represents a tumor. Data analyzed using non-parametric Mann-Whitney test (A-B, E, F, J, K) and t-test (C, D, H, I). *** $P \leq 0.001$ **** $P \leq 0.0001$.

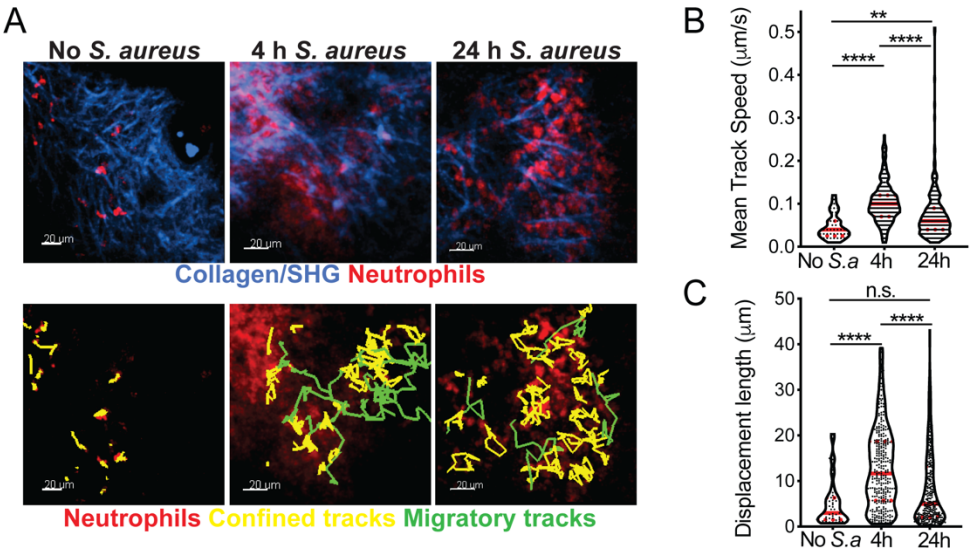

Figure 2. Tumor neutrophil dynamics in vivo. A. Neutrophils (red) were visualized in steady state or in S. aureus (S.a) bioparticle treated LLC tumors using intravital two-photon microscopy. Yellow tracks indicate neutrophils with confined motility (track displacement length<13mm), green tracks indicate migrating neutrophils (track displacement length>47 mm). Second Harmonic Generation (SHG)/collagen - blue. Bar represents 20 µm. B. Mean track speed of intratumoral neutrophils. C. Track displacement length of intratumoral neutrophils. Data from at least 4 independent imaging experiments per time point was analysed using a one-way ANOVA with Dunn's correction for multiple comparisons (B and C). Median and quartiles are shown. **P ≤ 0.01, **** P ≤ 0.0001, n.s. not significant.

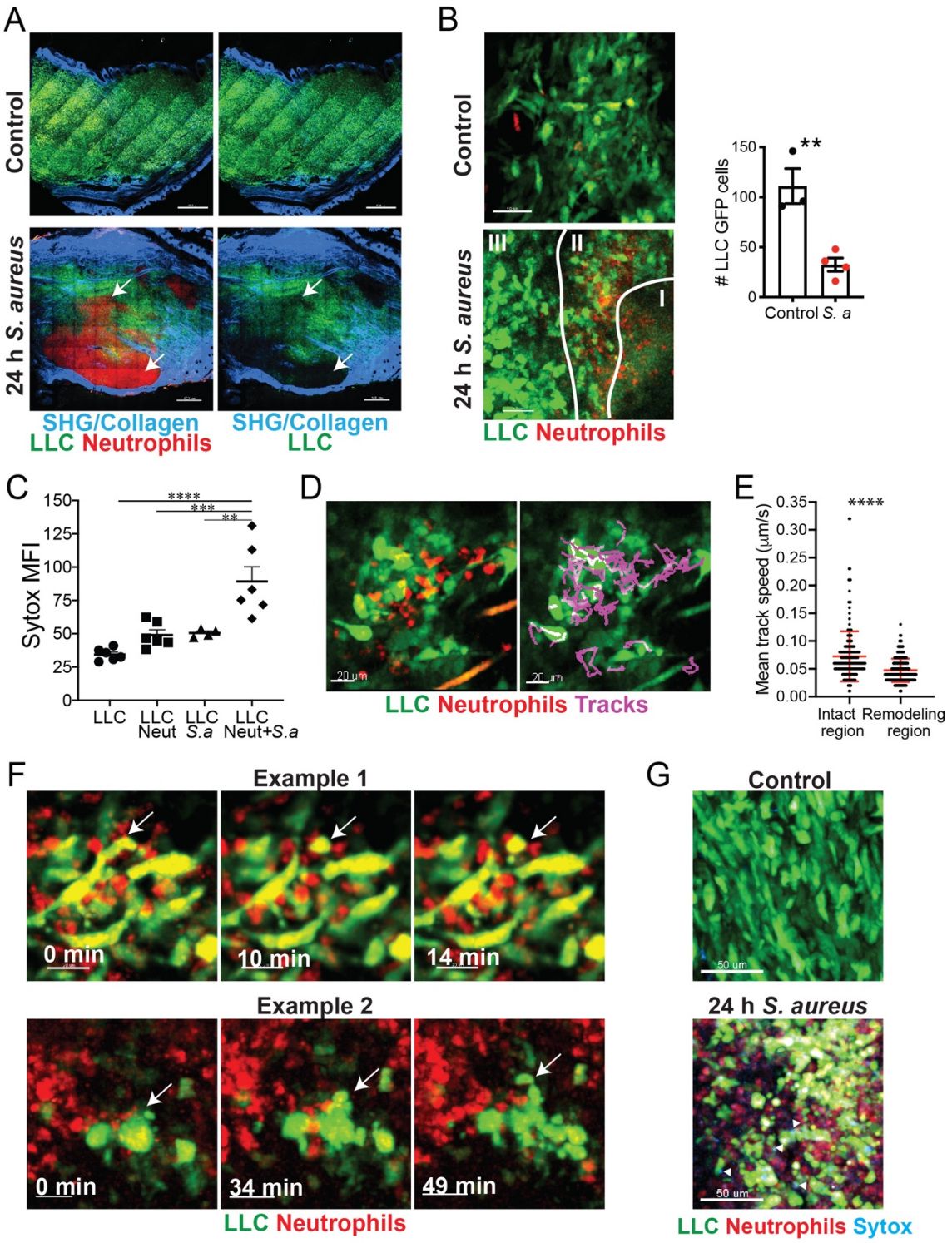

Figure 3. Visualizing neutrophil interactions with tumor cells. A. LLC-GFP tumor cells (green), neutrophils (red) and Second Harmonic Generation (SHG)/Collagen (blue) were visualized in frozen sections from bioparticle treated and control tumors using two-photon microscopy. White arrows indicate areas of tumor cell clearance by neutrophils. Scale bar represents 500 mm. B. Neutrophils (red) and LLC cells (green) were visualized in tumors prior or 24 h following S. aureus treatment using intravital microscopy. Region I indicates an area of LLC loss, region II: partial LLC destruction, region III: largely intact but rounded LLCs. Quantitation of LLC-GFP cell loss (right panel). C.

Killing of LLC-GFP cells was assessed using SYTOX labeling to detect dead cells 24 h following incubation with *S. aureus*-stimulated or control neutrophils *in vitro*. D. Purple tracks show neutrophils (red) interacting and crawling over LLC cells (green). Bar represents 20 µm. E. Quantitation of neutrophil motility in areas of intact tumor cells and areas extensive tumor remodeling and cell debris. F. Two examples of neutrophil-LLC interactions and tumor cell blebbing (white arrows). Bar represents 20 µm. G. LLC-GFP tumors (green), neutrophils (red) and SYTOX (blue) were visualized in frozen sections from bioparticle treated and control tumors using two-photon microscopy. White arrows indicate SYTOX staining of LLC cells. Scale bar represents 50 µm. Data analyzed using Mann-Whitney test (B, E) and one-way ANOVA (C). ** $P \leq 0.01$ *** $P \leq 0.001$ **** $P \leq 0.0001$

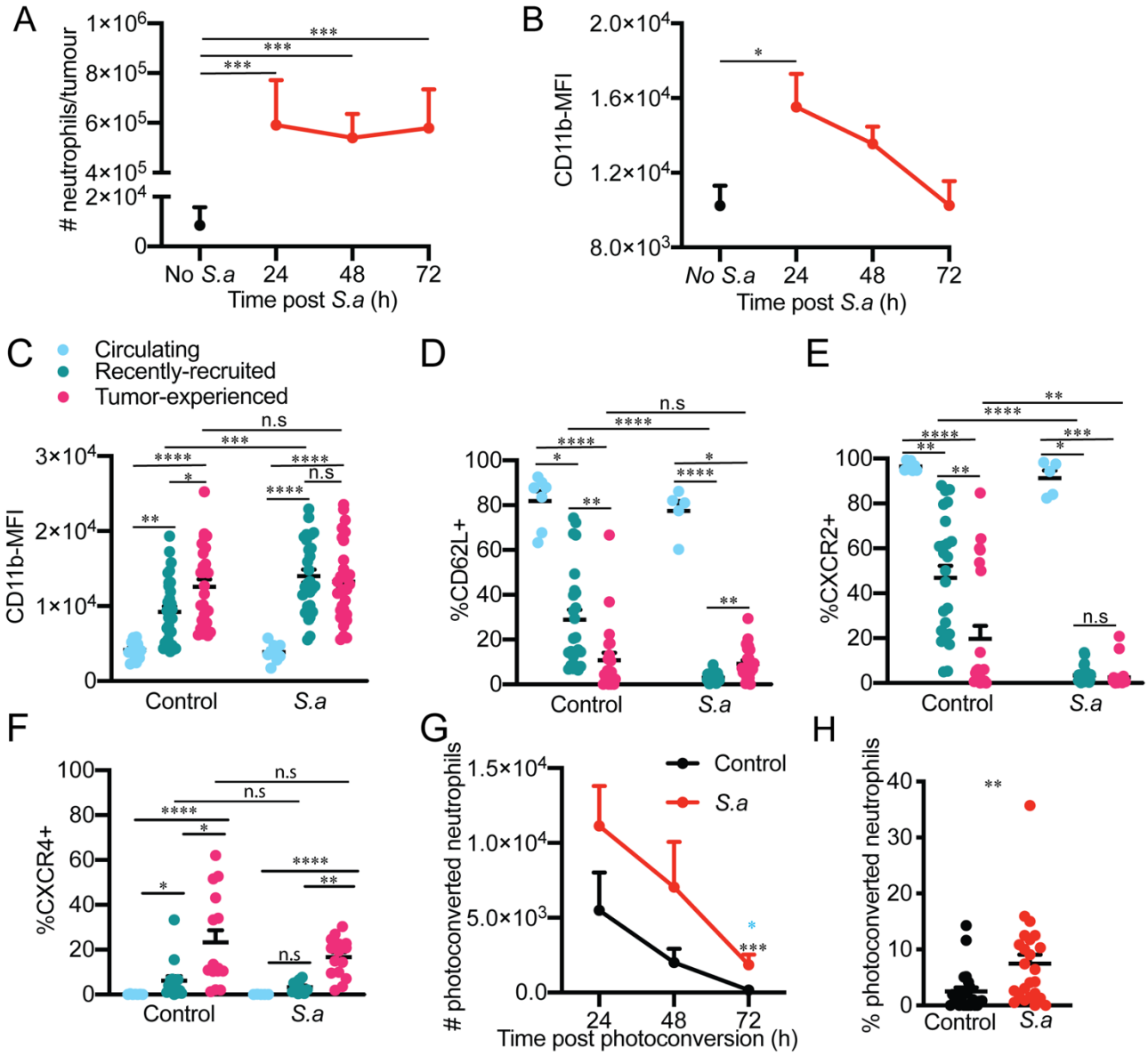

Figure 4. Modulation of tumor neutrophil phenotype and persistence by signals in the TME. Neutrophil number (A) and CD11b expression (B) over time after an injection of S. aureus bioparticles. Tumors were photoconverted and treated with S. aureus bioparticles and CD11b (C), CD62L (D), CXCR2 (E) and CXCR4 (F) expression was analyzed 24 h later on circulating (blue),

recently-recruited (non-photoconverted, green) and tumor-experienced (photoconverted, magenta) neutrophils using flow cytometry. G. Tumors were photoconverted and treated with S. aureus bioparticles immediately after photoconversion. Photoconverted neutrophils in tumors were quantified 24, 48 and 72 h later. H. Flow cytometric analysis of photoconverted neutrophils in tumor draining lymph 24 h after photoconversion. Each circle represents a tumor, blood or lymph node sample, mean +SEM are shown (C-E and H) or the mean+SEM of at least 7 tumor samples (G). Mean + SEM from data pooled from at least two independent experiments and analyzed using Kruskal-Wallis test (A, B, D-F), one-way ANOVA (C), multiple T-test (G) or Mann-Whitney test (H). * P≤0.05 ** P ≤ 0.01 *** P ≤ 0.001 **** P ≤ 0.0001. In (G) Blue * indicates 24 vs 72 h comparison, black * indicates S. aureus vs control comparison.

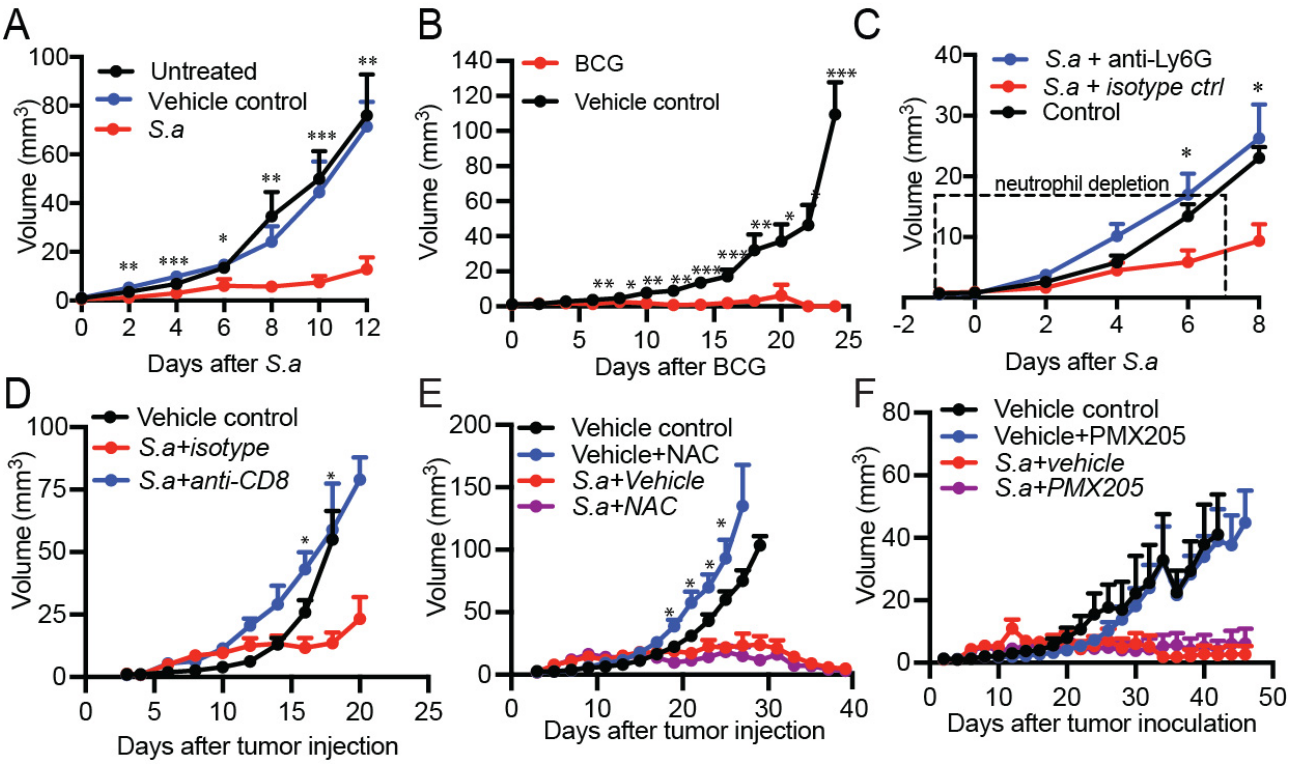

Figure 5. Microbial treatment leads to neutrophil-dependent inhibition of tumor growth. A. Tumor volume was measured in S. aureus, saline (vehicle) treated or untreated LLC, tumors grown in C57BL/6 mice and treated every second day. B. Tumor volume in BCG-treated or vehicle control LLC tumors in C57BL/6 mice. C. LLC tumor volume in C57BL/6 mice following anti-Ly6G neutrophil depletion on days -1, 1, 3, 5, 7. S. aureus was injected on days 0, 2, 4, 6, 8. D. LLC tumor volume following CD8+ T-cell depletion. Anti-CD8 was administered i.p. every 3 days and *S. aureus* every 2 days. E. AT3 tumor volume in C57BL/6 mice treated with N-*acetylcysteine* (*NAC*) to inhibit ROS. NAC was administered daily from time of tumor inoculation and *S. aureus* was injected every 2nd day once tumors were detectable. F. AT3 tumor volume in C57BL/6 mice treated with C5aR antagonist, PMX205, i.p. daily and *S. aureus* every 2nd day. Data shown as a mean + SEM from 5 (A), 2 (B-C), 1 (D-F) experiments. Data analyzed using Mann-Whitney (A-C, F) or t-test (D-E). No

significant difference between *S.a*+Vehicle and *S.a*.+ NAC (E) or *S.a*+Vehicle and *S.a*.+ PMX205, differences between Vehicle and NAC were significant as indicated on the graph (E). *P ≤ 0.05 ** P ≤ 0.01 *** P ≤ 0.001 **** P ≤ 0.0001.

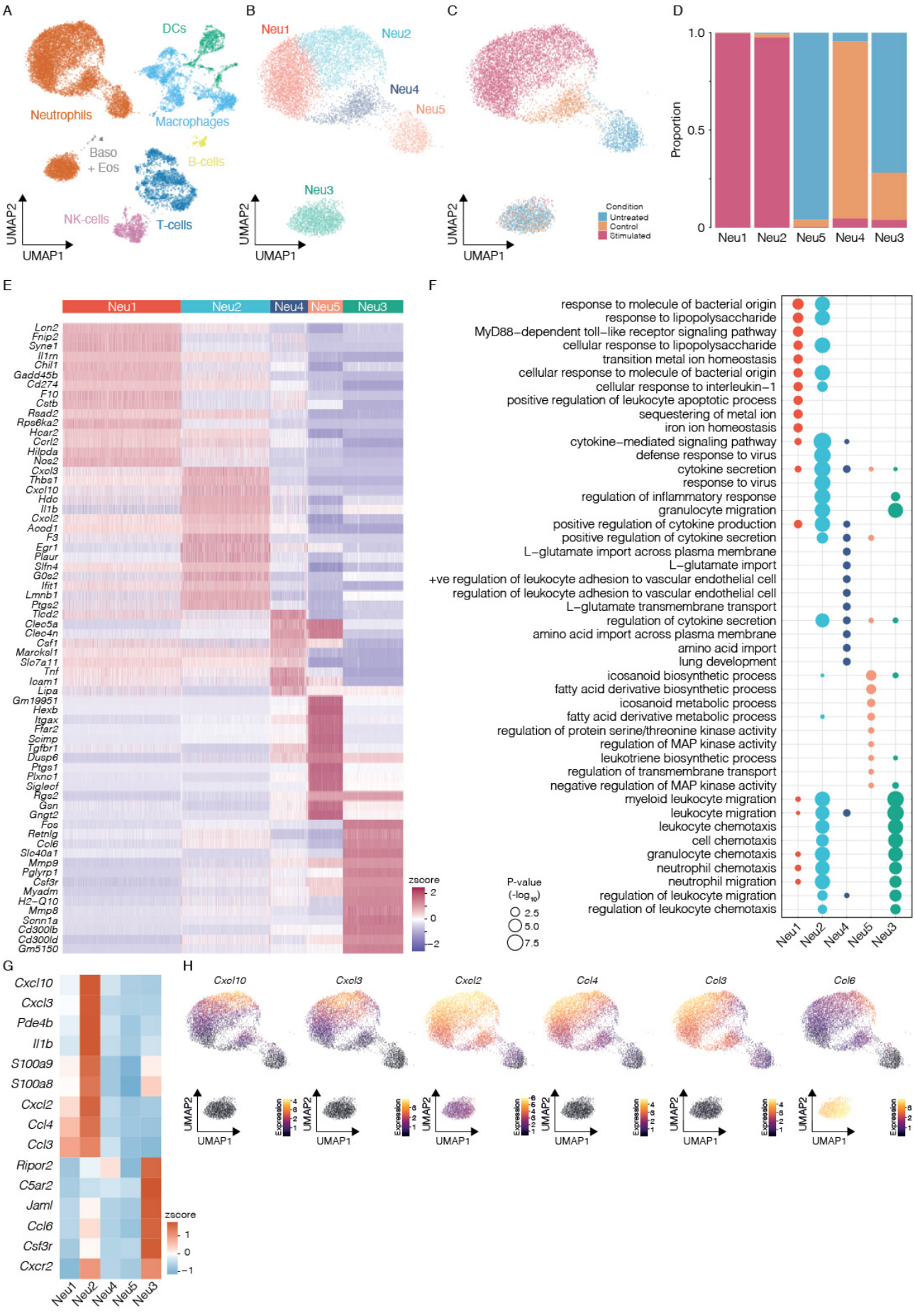
A
DCs
Neutrophils
Macrophages
Baso
+ Eos
B-cells
NK-cells
T-cells
UMAP2
UMAP1
B
Neu1
Neu2
Neu4
Neu5
Neu3
C
Condition
Untreated
Control
Stimulated
D
Proportion
1.0
0.5
0
Neu1
Neu2
Neu5
Neu4
Neu3
E
Neu1
Neu2
Neu4
Neu5
Neu3
Lcn2
Fnip2
Syne1
Il1rn
Chil1
Gadd45b
Cd274
F10
Cstb
Rsad2
Rps6ka2
Hcar2
Corl2
Hilpda
Nos2
Cxcl9
Thbs1
Cxcl10
Hdc
Il1b
Cxcl2
Acod1
F3
Egr1
Plaur
Slfn4
G0s2
Ifit1
Lmnb1
Ptgs2
Tlcd2
Clec5a
Clec4n
Csf1
Marcksl1
Slc7a11
Tnf
Icam1
Lipa
Gm19951
Hexb
Itgax
Ffar2
Scimp
Tgfbr1
Dusp6
Ptgs1
Plxnc1
Siglecf
Rgs2
Gsn
Gngt2
Fos
Retnlg
Ccl6
Slc40a1
Mmp9
Pglyrp1
Csf3r
Myadm
H2-Q10
Mmp8
Sonn1a
Cd300lb
Cd300ld
Gm5150
zscore
2
0
−2
F
response to molecule of bacterial origin
response to lipopolysaccharide
MyD88−dependent toll−like receptor signaling pathway
cellular response to lipopolysaccharide
transition metal ion homeostasis
cellular response to molecule of bacterial origin
cellular response to interleukin−1
positive regulation of leukocyte apoptotic process
sequestering of metal ion
iron ion homeostasis
cytokine−mediated signaling pathway
defense response to virus
cytokine secretion
response to virus
regulation of inflammatory response
granulocyte migration
positive regulation of cytokine production
positive regulation of cytokine secretion
L−glutamate import across plasma membrane
L−glutamate import
+ve regulation of leukocyte adhesion to vascular endothelial cell
regulation of leukocyte adhesion to vascular endothelial cell
L−glutamate transmembrane transport
regulation of cytokine secretion
amino acid import across plasma membrane
amino acid import
lung development
icosanoid biosynthetic process
fatty acid derivative biosynthetic process
icosanoid metabolic process
fatty acid derivative metabolic process
regulation of protein serine/threonine kinase activity
regulation of MAP kinase activity
leukotriene biosynthetic process
regulation of transmembrane transport
negative regulation of MAP kinase activity
myeloid leukocyte migration
leukocyte migration
leukocyte chemotaxis
cell chemotaxis
granulocyte chemotaxis
neutrophil chemotaxis
neutrophil migration
regulation of leukocyte migration
regulation of leukocyte chemotaxis
P-value
(-log10)
2.5
5.0
7.5
Neu1
Neu2
Neu4
Neu5
Neu3
G
Cxcl10
Cxcl3
Pde4b
Il1b
S100a9
S100a8
Cxcl2
Ccl4
Ccl3
Ripor2
C5ar2
Jaml
Ccl6
Csf3r
Cxcr2
zscore
1
0
−1
Neu1
Neu2
Neu4
Neu5
Neu3
H
Cxcl10
Cxcl3
Cxcl2
Col4
Col3
Col6
UMAP2
UMAP1
Expression

Figure 6. Neutrophils in the TME acquire an activated transcriptional state and upregulate cytokines following microbial stimulation. A. UMAP embedding of TME immune cell populations profiled by single cell sequencing. B. UMAP embedding of neutrophil populations Neu1-5. C. Overlay of experimental conditions (Unmanipulated, Vehicle control, *S. aureus* treated), otherwise as in B. D. Stacked bar plot of proportion of cells from three experimental conditions across Neu1-5. E. Heatmap of scaled smoothed expression for the top 15 marker genes for Neu1-5 based on fold enrichment, with columns and rows representing cells and genes, respectively. F. Bubble plot of top biological processes enriched among marker genes for Neu1-5. Bubbles represent gene significant terms (FDR < 0.05, 1-sided Fisher's exact test) with size reflecting $-\log_{10}$(P-value). G. Heatmap of scaled mean expression aggregated by cell state Neu1-5 for marker genes involved in chemotaxis (Gene Ontology term Neutrophil Chemotaxis GO:0030593 and C5ar2, Ripor2). H. UMAP embeddings colored by smoothed expression of chemokines identified as marker genes.

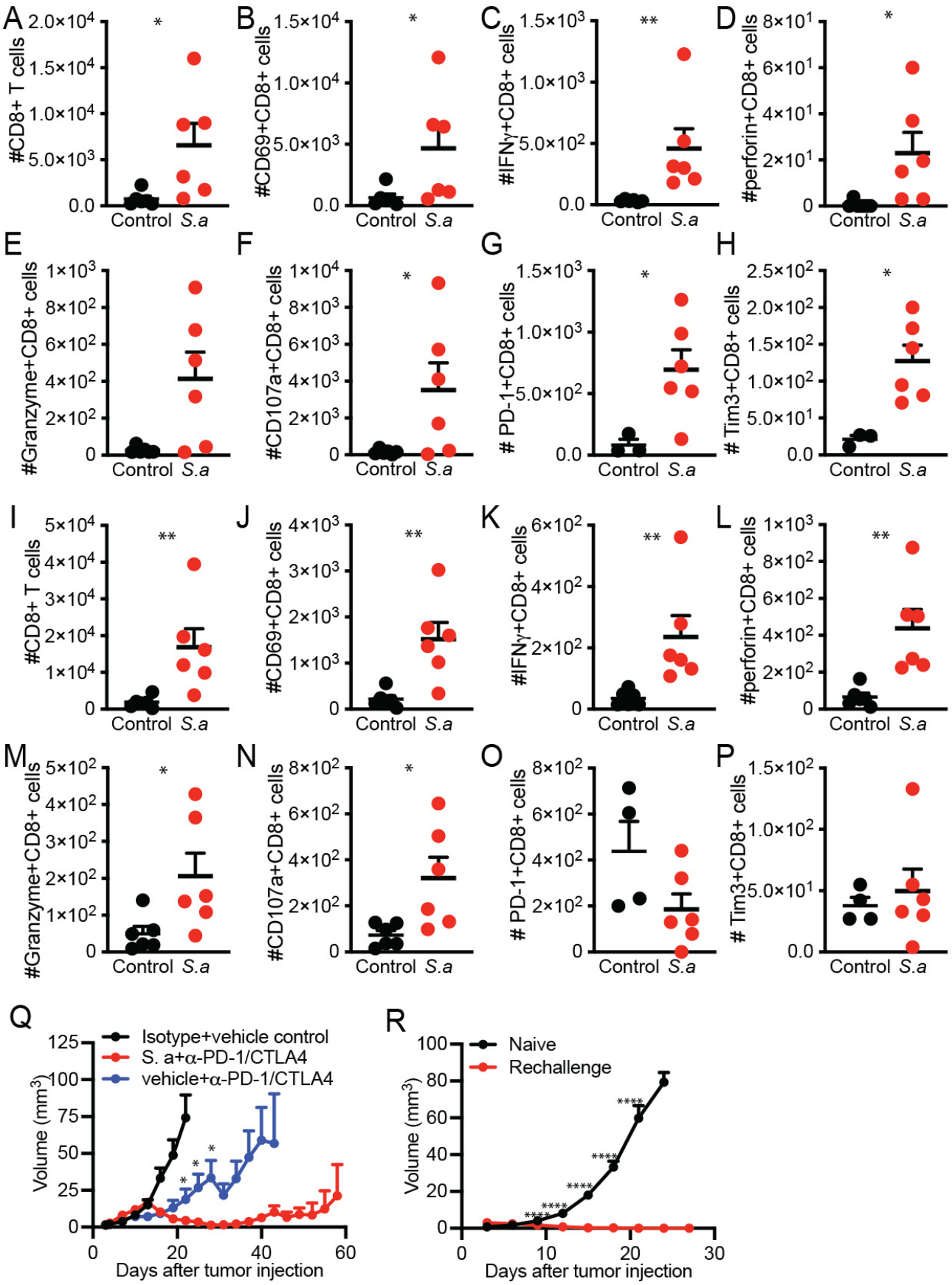

Figure 7. Microbial therapy enhances CD8 effector function and response to checkpoint inhibitor therapy. CD8 T cell number, activation and effector markers in LLC tumors (A-H) and

draining lymph nodes (I-P) following 2 rounds of S. aureus bioparticle administration 2 days apart assessed 72 h after the last treatment. Expression of CD69 (B/J), IFNγ (C/K), perforin (D/L), granzyme, CD107 (E/M), PD-1 (F/N) and TIM3 (H/P) in tumor/lymph node CD8 T cells. Q. Tumor volume in C57BL/6 mice bearing at AT-3 tumors that have previously received AT-3 cells and were treated with microbial therapy to suppress tumor growth and rested for at least 60 days or tumor naive mice. Data shown as mean + SEM with each circle representing one tumor or lymph node (A-P) or at least 4 tumors per timepoint (Q-R). Data analyzed using Mann-Whitney (A-E, G-R) or t-test (F). * P $\leq$0.05 ** P $\leq$ 0.01 **** P $\leq$ 0.0001.

SUPPLEMENTARY FIGURE LEGENDS:

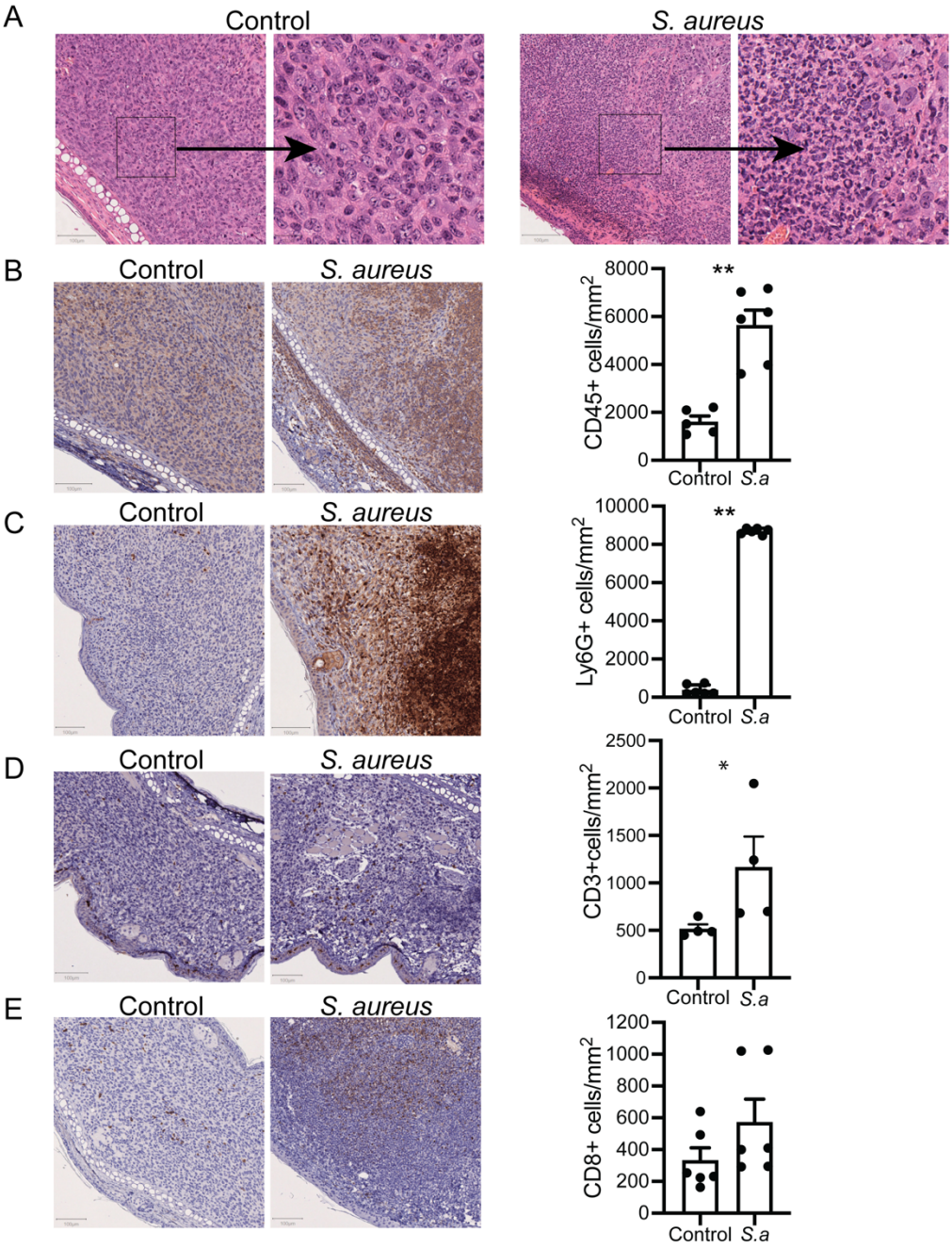

Supplementary Figure 1. Immunohistochemistry analysis of microbe-driven recruitment of immune cells into tumors. A. Recruitment of CD45+ leukocytes (B), Ly6G+ neutrophils (C), CD3+ (D) and CD8+ T cells (E) was assessed by immunohistochemistry on tumor sections 24 h post *S. aureus* injection into LLC tumors. Scale bars represent 100 µm and 20 µm for insets in (A). Mean + SEM of at least 3 different tumors is shown. Data analyzed with non-parametric Mann-Whitney test ** $P \leq 0.01$.

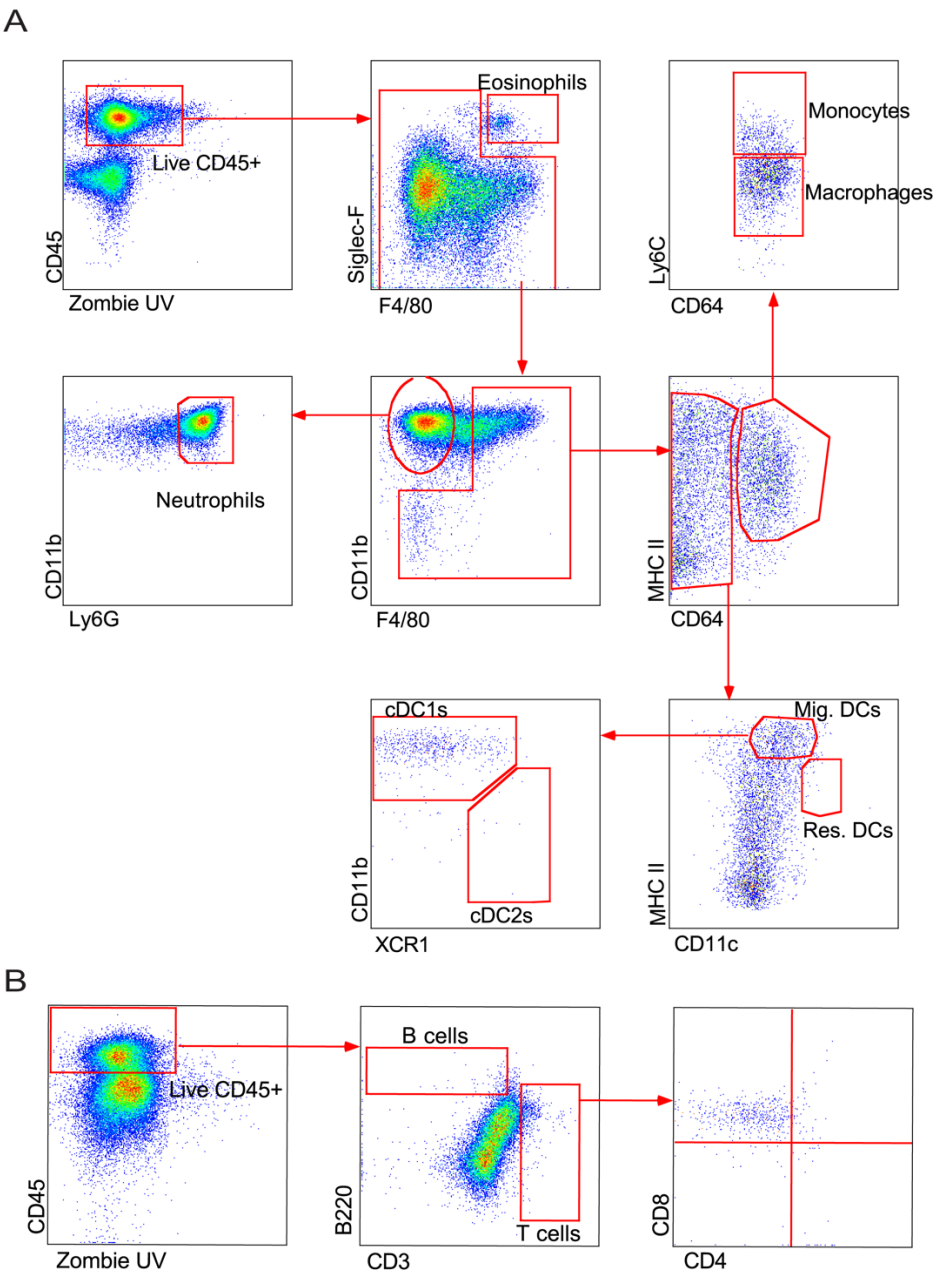

Supplementary Figure 2. Gating strategy for flow cytometric analysis of leukocyte infiltration into tumors. A. Representative dot plots from flow cytometric analyses showing gating strategy for neutrophils, eosinophils, monocytes, macrophages, and DCs in LLC tumors. FACS gating strategy was SSC-A/FSC-A (leukocytes), FSC-H/FSC-A (single cells), CD45/Zombie UV (Live CD45+ cells), Siglec-F/ F4/80 (Siglec-F+ F4/80+ eosinophils), CD11b/ F4/80, then CD11b/Ly6G in CD11b+ F4/80- for CD11b+ Ly6G+ neutrophils. In non-CD11b+ F4/80- cells, MHC II/CD64, then for CD64+

cells, Ly6C/CD64 (Ly6Chigh monocytes, Ly6Cintermediate/low macrophages). For CD64- cells, MHC II/CD11c for migratory and resident DCs, then CD11b/XCR1 in migratory cells for cDC1s and cDC2s. B. Representative dot plots from flow cytometric analyses showing gating strategy for T cells in intradermal LLC tumors 24 hours or 7 days after treatment with S. aureus. FACS gating strategy was SSC-A/FSC-A (leukocytes), FSC-H/FSC-A (single cells), CD45/Zombie UV (Live CD45+ cells), B220/CD3 (B & T cells), CD8/ CD4 (CD8 and CD4 T cells).

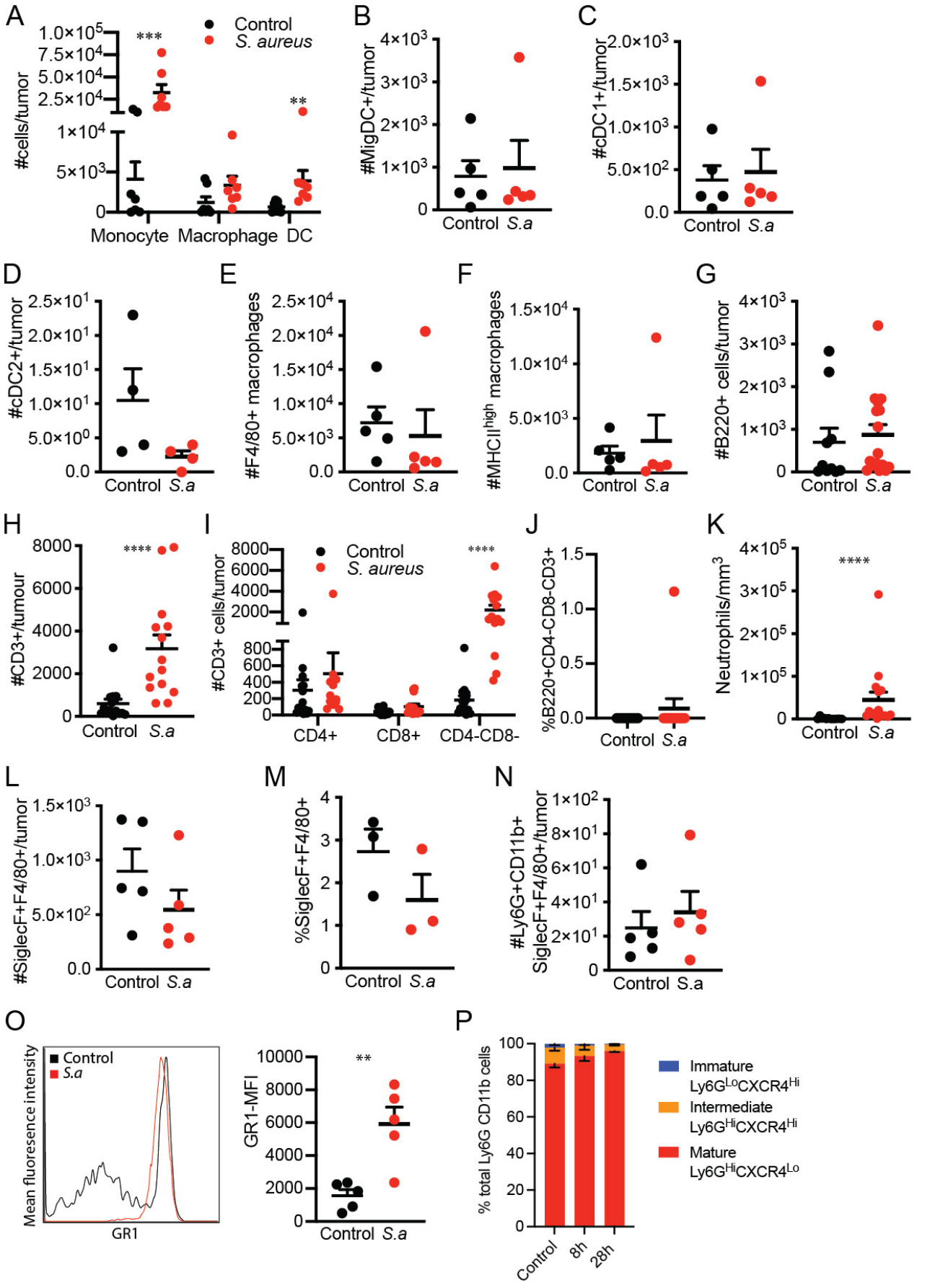

Supplementary Figure 3. Characterization of microbe-driven recruitment of immune cells into tumors. Recruitment of myeloid immune cells (A), migDCs (B), cDC1s (C), cDC2s (D), F4/80+

macrophages (E), MHCII^{high} macrophages (F), B220+ B cells (G), CD3+ T cells (H) and their subsets (I), proportion of CD3+CD4-CD8- that express B220+ (J) in LLC tumors 24 h after *S. aureus* injection. K. Number of neutrophils per tumor volume (per mm^3). SiglecF+F4/80+ eosinophils in tumors (L) and percentage of circulating SiglecF+F4/80+ eosinophils in blood (M) and the number of Ly6G+CD11b+SiglecF+F4/80+ cells per tumor (N) 24h after *S. aureus* injection into LLC tumors. MFI of GR-1+ myeloid immune cells (CD45+CD11b+F4/80-) (O) and the proportion of CXCR4 and Ly6G subsets out of total Ly6G+ CD11b+cells 24 h after *S. aureus* injection into LLC tumors (P). Mean + SEM of one (B-F, L-O), two (A, P) and three (G, J-K) independent experiments. Data analyzed with non-parametric Mann-Whitney test (A-C, E-K), parametric T-test (D, K-N), non-parametric Kruskal-Wallis test (O). ** $P \leq 0.01$*** $P \leq 0.001$ **** $P \leq 0.0001$

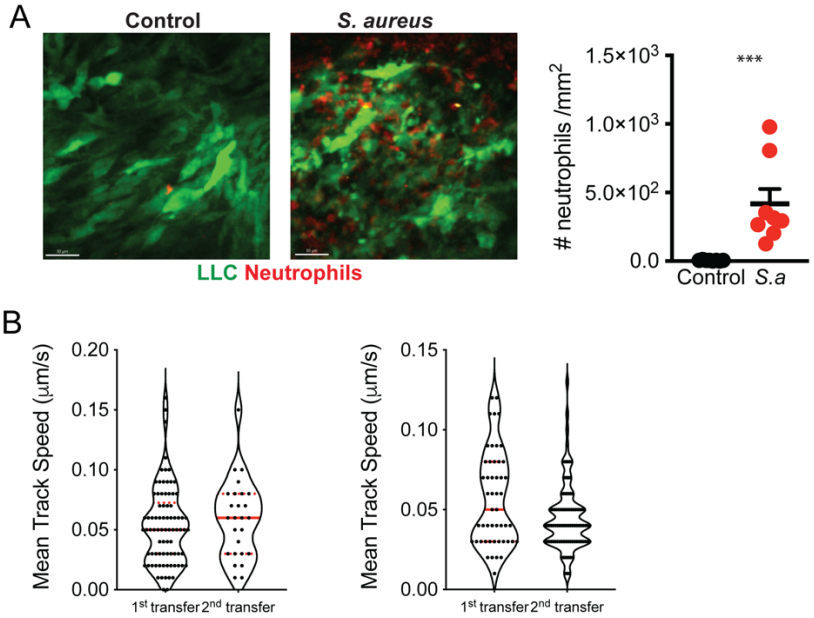

Supplementary Figure 4. Recruitment of adoptively transferred neutrophils in response to microbial therapy. Bone marrow cells from BigRed/Catchup$^{IVM\text{-}red}$ mice were adoptively transferred into tumor bearing C57BL/6 mice 10 days after tumor inoculation, and S. aureus bioparticles were administered immediately after transfer. Neutrophils (red) and LLC tumor cells (green) were visualized in steady state or 24 h after *S. aureus* bioparticle treatment using intravital two-photon microscopy. Scale bar represents 30μm. Quantitation of recruitment of adoptively transferred neutrophils (right panel). B. Lysozyme M tdTomato bone marrow cells were transferred into C57BL/6 mice on day 10 of LLC tumor growth. 24 h later, lysozyme M kikume green bone marrow cells were transferred into the same C57BL/6 mice that had previously received Lysozyme M tdTomato bone marrow cells. Following the second transfer, neutrophil motility was visualized using intravital two-photon microscopy at 2 h and 24 h. There was no significant difference in mean track

speed between the two groups of neutrophils, whether imaged immediately following the 2nd transfer (left panel), or 24 h after the 2nd transfer (right panel).

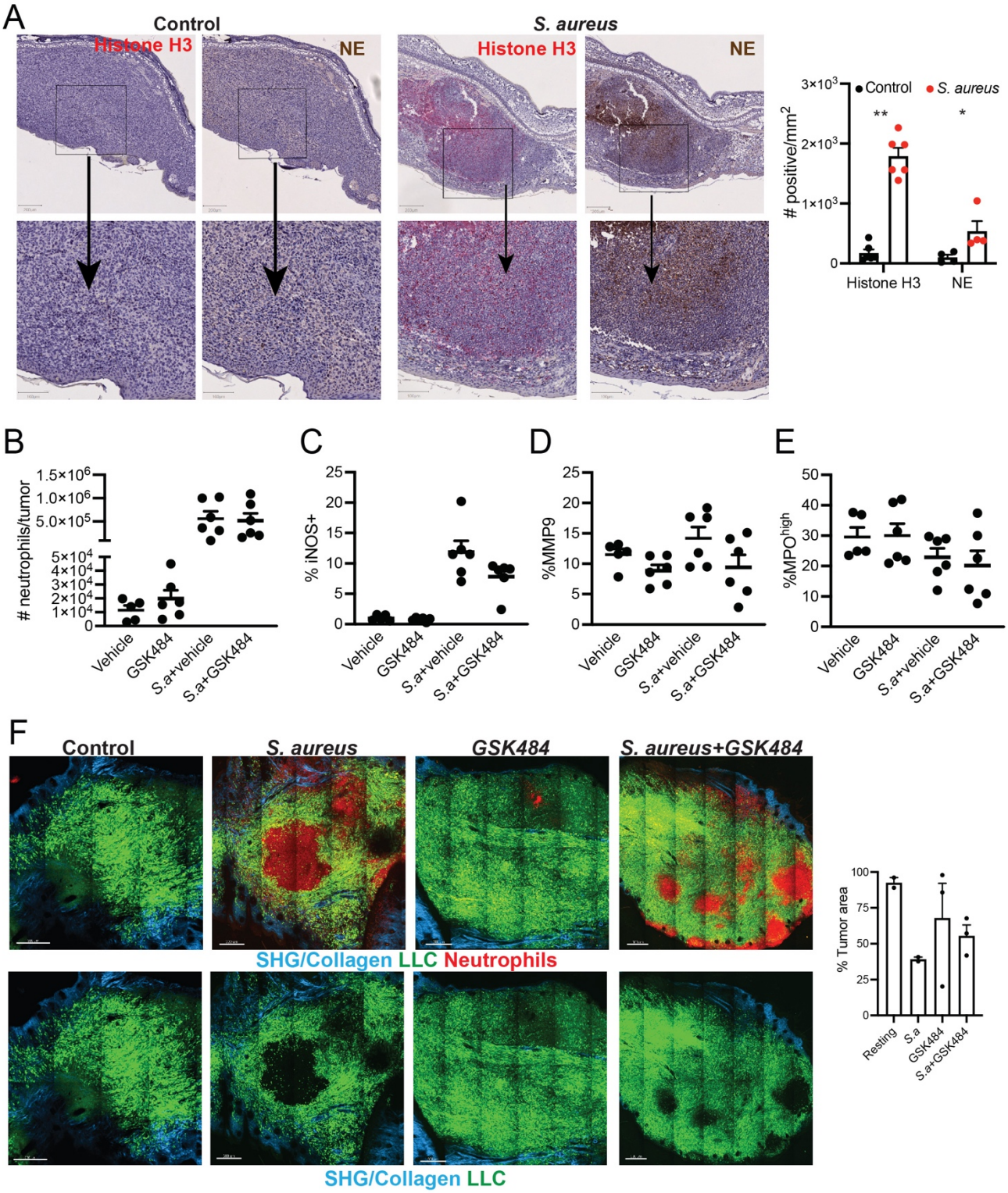

Supplementary Figure 5. NETs generation by tumor neutrophils in response to microbial treatment. A. Histone H3 and NE expression in unmanipulated LLC tumors, and in LLC tumors following S. aureus treatment. Scale bar in upper panels represents 200um. Scale bar in lower panels represent 100um. Quantitation of histone H3 and NE expression (right panel). B-E. LLC-GFP tumor

cells (green), neutrophils (red) and Second Harmonic Generation (SHG)/Collagen (blue) were visualized in frozen sections from tumors treated with bioparticles +/- the PAD4 inhibitor GSK484, tumors with GSK484 alone, and control tumors using two-photon microscopy. Scale bar represents 300um. Quantitation of area occupied by tumor cells in each treatment group (right panel). Mean + SEM of at least 2 different tumors is shown. There was no significant difference between S. aureus treatment alone versus S. aureus + GSK484.

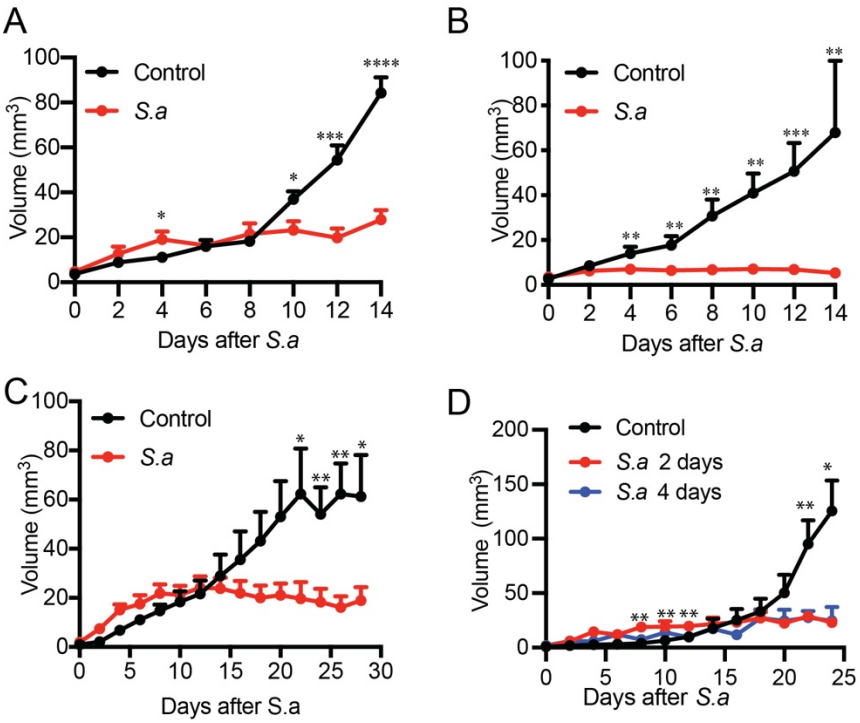

Supplementary Figure 6. Microbial treatment alters tumor growth in different tumor models. Tumor volume was measured in S. aureus treated or control mice bearing B16F10 3C (A), AT3 (B) or KPC (C) tumors and treated every second day. D. Tumor volume in *S. aureus*- or vehicle-treated LLC tumors in C57BL/6 mice treated every 2nd or every 4th day. Data shown as mean + SEM of at least 3 tumors and representative of 2 independent experiments. Data analyzed using Mann-Whitney test (A, D) or t-test (B) * P ≤0.05 ** P ≤ 0.01 *** P ≤ 0.001 **** P ≤ 0.0001.

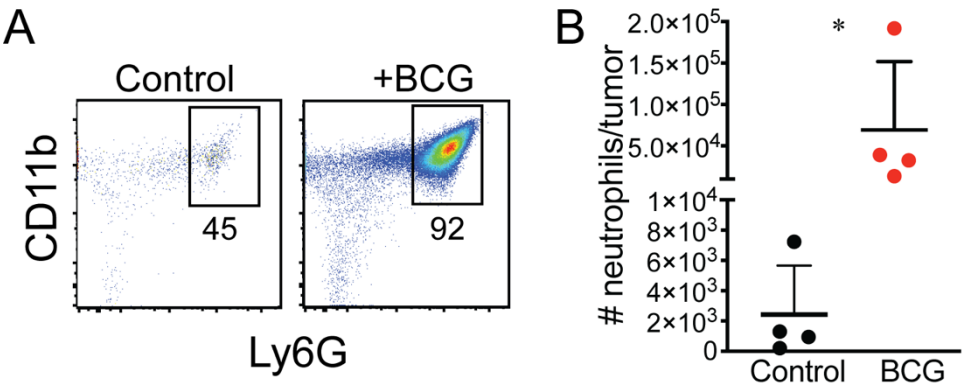

Supplementary Figure 7. BCG-driven recruitment of intratumoral neutrophils. BCG injection into tumors leads to an influx of neutrophils into LLC tumors. A. Representative flow cytometry plots 24 hours post BCG treatment. B. Neutrophil number in LLC tumors. Each circle represents a single tumor. Data is from one experiment and analyzed using non-parametric Mann-Whitney test. * P <0.05.

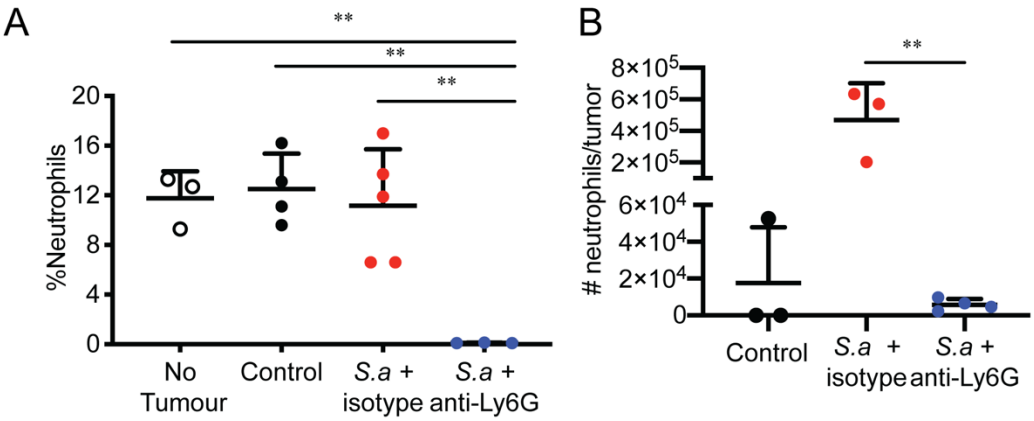

Supplementary Figure 8. Neutrophil depletion with anti-Ly6G antibody. A. Circulating neutrophils were analyzed in C57BL/6 mice with LLC tumors. Neutrophils were depleted with anti-Ly6G (clone 1A8) 1 day prior and 1 day following S. aureus bioparticle treatment. Blood was collected 24 h later. B. Neutrophils were depleted as in (A) and then mice received alternating anti-Ly6G treatment and *S. aureus* treatment for next 72 h. Mice were sacrificed 24 h later and tumor neutrophils were analyzed using flow cytometry. Neutrophils were quantitated using CD11b and unlabeled anti-Ly6G antibody as well as a secondary antibody to detect anti-Ly6G in the staining mix and remaining antibody from depletion treatments. Means + SEM are shown. Each dot represents a single mouse (A) or tumor (B). Data was analyzed using one-way ANOVA ** $P \leq 0.01$

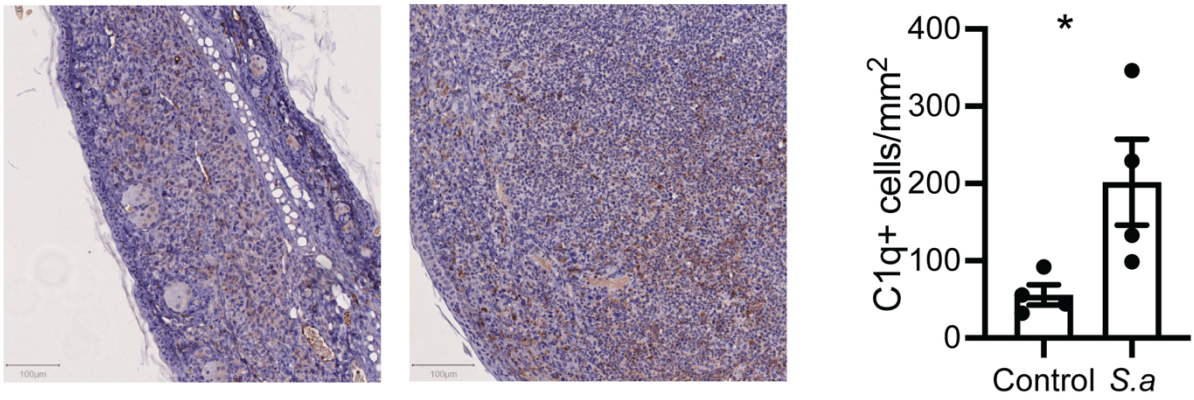

Supplementary Figure 9. C1q expression following microbial treatment. C1q expression was assessed by immunohistochemistry on tumor sections 24 h post S. aureus injection into LLC tumors. Mean + SEM is shown, each circle represents a single tumor. Data analyzed with non-parametric Mann-Whitney test ** $P \leq 0.01$

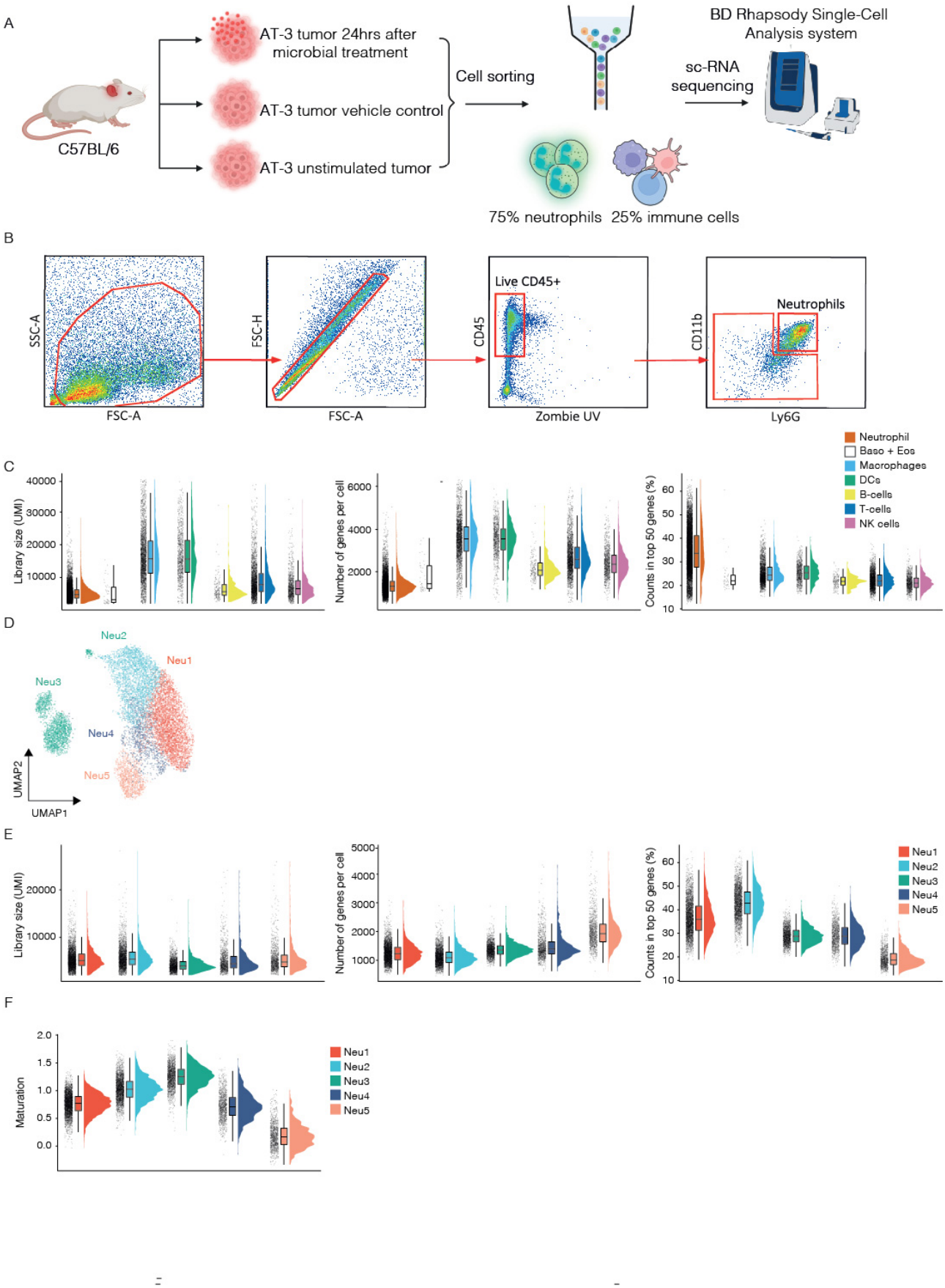

Supplementary Figure 10. Single cell analysis of TME immune populations. A. Schematic representation of experimental workflow for single cell transcriptional analysis of tumor immune cell response to microbial therapy. FACS sorted single-cell suspensions from AT-3 tumors 24hrs after S.

aureus bioparticle treatment (n=5 mice), vehicle control (n=5 mice) and unmanipulated (n=5 mice) tumors were pooled to obtain a ratio of 75% neutrophils to 25% non-neutrophil CD45+ immune cells and sequenced with BD Rhapsody Single-cell analysis system. B. Representative flow cytometry plots illustrating cell sorting strategy. C. Rain cloud plots of per-cell summary statistics across immune populations Neutrophils, Basophils and Eosinophils (Base + Eos), Macrophages, Dendritic cells (DCs), B-cells, T-cells, NK cells. Shown are library size (total unique molecular identifiers (UMIs) per cell) (left), number of genes detected (center), percent of UMIs in top 50 most highly expressed genes (right). D. UMAP embedding of neutrophil populations after batch correction with colors indicating neutrophil state based on uncorrected data. E. Rain cloud plots of per-cell summary statistics across neutrophil states Neu1-5, otherwise as in C. F. Rain cloud plots of per-cell maturation score across neutrophil states Neu1-5.

SUPPLEMENTARY TABLE LEGENDS:

Supplementary Table 1. Characterization of neutrophil populations in single cell analysis. Marker genes for neutrophil populations Neu1-5 (log fold change > 1) and gene ontology (GO) biological process (BP) terms enriched among marker genes for Neu1-5 (FDR < 0.05, 1-sided Fisher's exact test). Columns for marker spreadsheets are as follows: cluster - Cell population for which marker pertain, gene - Gene Symbol, Ensembl - Ensembl gene ID, p_val - Uncorrected p-value, avg_logFC - Log fold change in expression in cells from the cluster compared to cells outside of the cluster, pct.1 - the percentage of cells within cluster in which the gene is detected, pct.2 - the percentage of cells outside the cluster in which the gene is detected, p_val_adj - FDR adjusted p-value. Columns for GOBP spreadsheets are as follows: ID - GO term ID, Description - GO term description, Hits - Number of marker genes associated with GO term, Sampled - Number of marker genes associated with any GO term, Total_Hits - Number of genes expressed in the dataset associated with GO term, Background - Number of genes expressed in the dataset associated with any GO term, pvalue - Uncorrected p-value, p.adjust - FDR corrected p-value, geneID - List of marker genes associated with GO term, FE - Fold enrichment of marker genes associated with GO term as per Hits/(Sampled*Total_Hits/Background).

SUPPLEMENTARY VIDEO LEGENDS:

Video 1. Neutrophil migration before and after microbial bioparticle treatment. Ly6G neutrophil (red) migration in intact unmanipulated LLC tumors (part 1) and tumors that were treated with *S. aureus* bioparticles 4 and 24 hours earlier (part 2 and 3 respectively). Tracks indicate neutrophil paths. Yellow tracks indicate neutrophils with restricted motility (track displacement length less than 13 μm), green tracks indicate more motile neutrophils (track displacement length greater than 47 μm). Collagen/Second harmonic generation (SHG, blue). Projection of a time-lapse series imaged in LLC tumors in the ear flap of BigRed/Catchup$^{IVM\text{-}red}$ mice. Part 1 dimensions: 213 μm x 213 μm x 45 μm x 20 minutes. Images were taken 30 seconds apart; Part 2 dimensions: 166 μm x 166 μm x 93 μm x 30 minutes. Images were taken 30 seconds apart; Part 3 dimensions: 191 μm x 191 μm x 24 μm x 48 minutes. Images were taken 60 seconds apart. Elapsed time is shown as days:hours:min:seconds.

Video 2. Neutrophil interactions with LLC cells in unmanipulated and treated tumors. Part 1: Intact elongated LLC (green) cells in unmanipulated tumors with scattered Ly6G neutrophils (red). Part 2: LLC cells progressively lose their elongated appearance to become rounded and then be broken down by Ly6G neutrophils. Projection of a time-lapse series imaged in eGFP-LLC tumors in the ear flap of BigRed/Catchup$^{IVM\text{-}red}$ mice. Part 1 dimensions: 249 μm x 249 μm x 105 μm x 20 minutes. Images were taken 30 seconds apart; Part 2 dimensions: 249 μm x 249 μm x 105 μm x 49 minutes. Images were taken every 60 seconds. Elapsed time is shown as days:hours:min:seconds.

Video 3. Neutrophils engage in multiple interactions with LLC tumor cells following microbial bioparticle treatment. Two-photon microscopy was used to visualize Ly6G neutrophil (red) interacting with LLC cells (green) 24 hours after microbial bioparticle treatment. Magenta tracks indicate neutrophil paths. Projection of a time-lapse series imaged in eGFP-LLC tumors in the ear flap of BigRed/Catchup$^{IVM\text{-}red}$ mice. Dimensions: 166 μm x 166 μm x 63 μm x 20 minutes. Images were taken 30 seconds apart. Elapsed time is shown as days:hours:min:seconds.

Video 4. Neutrophil interactions with LLC cells lead to tumor cell blebbing. Two-photon microscopy was used to visualize Ly6G neutrophil (red) interactions with LLC cells (green) 24 hours following microbial bioparticle treatment. Projection of a time-lapse series imaged in eGFP-LLC tumors in the ear flap of BigRed/Catchup$^{IVM\text{-}red}$ mice. Example 1 dimensions: 125 μm x 125 μm x 93 μm x 60 minutes. Example 2 dimensions: 125 μm x 125 μm x 78 μm x 60 minutes. Images were taken every 60 seconds. Elapsed time is shown as days:hours:min:seconds.